1-1-2015

Enhancement In Electrochemical Performance Of Advanced Battery Electrodes Using Carbon-Nanomaterial Composites

Kulwinder Dhindsa
Wayne State University,

ENHANCEMENT IN ELECTROCHEMICAL PERFORMANCE OF LiFePO$_4$-CARBON NANO COMPOSITE MATERIALS FOR LITHIUM ION BATTERIES

by

KULWINDER S. DHINDSA

DISSERTATION

Submitted to the Graduate School of

Wayne State University,

Detroit, Michigan

in partial fulfillment of the requirements

for the degree of

DOCTOR OF PHILOSOPHY

2015

MAJOR: PHYSICS

Approved by:

_____

Advisor   Date

_____

_____

_____

DEDICATION

'To my loving family, especially my father and late mother'

ACKNOWLEDGEMENTS

TABLE OF CONTENTS

LIST OF TABLES

LIST OF FIGURES

CHAPTER 1

INTRODUCTION AND MOTIVATION

1.1 Need for high-energy storage system

Energy storage is the storage of some form of energy that can be drawn upon at a later time to perform some useful operation. The electrochemical energy storage devices generally include batteries and super-capacitors. Due to shortage of fossil fuels, these systems need to be developed to meet the energy requirements, especially in automotive areas. It is a matter of fact that semi or fully electric vehicles should replace traditional combustion engine motor vehicles. There are many advantages of hybrid and electric vehicles including:

- ❖ Zero tailpipe emissions (no CO_2 or other pollutants), particularly when they run in electrical mode.
- ❖ Use of cleaner electrical energy produced through advanced natural gas and coal gasification technologies
- ❖ Energy security by displacing imported petroleum with domestic generated electricity
- ❖ Overnight battery recharging (by plugging into a standard 110-volt household electric outlet or a higher voltage charging unit)
- ❖ Recycled energy from regenerative braking
- ❖ Lower fuel consumption and overall operational costs
- ❖ Possible use in secondary markets of the used batteries and reduced waste
- ❖ Less noise
- ❖ Low maintenance

1.2 Batteries and other electrochemical systems

Energy storage devices are characterized by two main parameters: Specific Power density and Specific Energy density. Figure 1.1 shows various types of storage devices in terms of their specific power density and
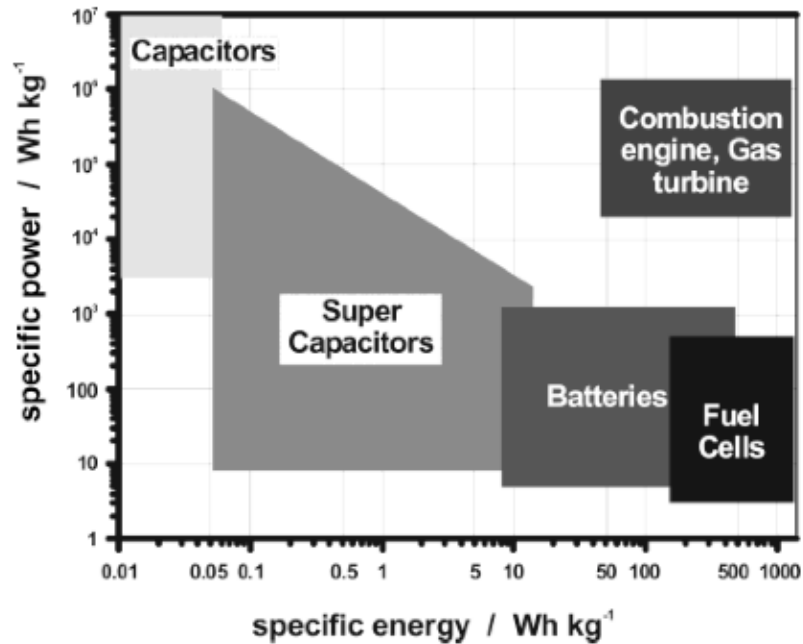
Figure 1.1 Specific Power and Specific Energy for various systems [1]

energy density. Combustion engines, fuel cells, batteries and super capacitors are the major energy sources being used to power these vehicles. Combustion engines are the best in terms of specific power as well as specific energy. But major disadvantages include limited amount of crude oil and environmental impact due to pollution of all kinds. Fuel cell has high specific energy but relatively low specific power and limited service life, whereas capacitors are known for their high power capability and long cycle life. A lot of research is being done on these types of energy conversion sources. Fuel cells are expensive due to materials and components cost, as well as challenges of storing hydrogen on board. In addition, fuel cell cannot store re-generative breaking energy. If we want to use a fuel cell in vehicles, its cost has to come down by a factor

of 10. It also relies on hydrogen fuel that requires distribution infrastructure and costly to produce from electrolysis, and water splitting processes. In the case of capacitors, the amount of energy stored per unit weight is considerably lower than that of an electrochemical battery (3-5 Wh/kg for an ultra-capacitor compared to 30-40 W·h/kg for a conventional battery). It is also important to note that ultra-capacitor has only about 10^{-4} times the volumetric energy density of gasoline. Batteries have attracted much interest in the past two decades. As in most of the batteries, materials are more abundant and at lower cost than those used in fuel cell. Furthermore, batteries have higher energy density than supercapacitors. In recent years, research to improve advanced batteries has dominated the energy storage research.

The transportation sector is the major user of the primary fuels. If somehow we can improve the power density and energy density of these batteries, they can be used in Hybrid Electric Vehicles (HEV's) and Electric Vehicles (EV's) to curtail the heavy consumption of the primary fuels and contribute to the reduction of green house gases. An ideal battery for transportation should have the following properties:

- ❖ A very high specific power capability during both charging and discharging

- ❖ Low cost at the cell, the module, and the pack levels

- ❖ A wide operating temperature range (-40°C to more than 80°C)

- ❖ Long cycle life, particularly for hybrid vehicles

- ❖ Long life, ideally 15 years, or life of a vehicle

- ❖ High reliability and high margin of safety

- ❖ A high usable energy density ratio (high use of State of Charge window) to increase autonomy

1.3 Classification of Batteries

A battery is an electrochemical device that can convert stored chemical energy to electrical energy. The transfer of electrons takes place from one material to another through an external electric circuit. This transfer of electrons results in the oxidation of a reducing agent (the anode) and the reduction of an oxidizer (the cathode), a process called oxidation-reduction or Redox reaction. Anode and cathode are separated by an ionically conductive separator containing electrolyte. The combination or stacking of anode, cathode and electrolyte is called a cell. A battery is made from many cells connected in parallel and/or in series depending upon the voltage and energy density requirements. Batteries are classified into two main categories-primary and secondary batteries.

1.3.1 Primary Batteries

Primary batteries are disposable and cannot be recharged. Once all the chemicals in this type of batteries are converted, they cannot be used anymore and must be recycled.

1.3.2 Secondary batteries

Batteries that can be recharged once discharged are considered as secondary batteries. These batteries are more cost effective as they can be used for longer time based on their cycle life. Most widely used secondary batteries are lead-acid batteries. But there are many disadvantages of lead-acid batteries. Due to the usage of heavy lead on anode and lead dioxide cathode, the energy density of lead-acid battery is very low (20-30 Wh/kg). In addition, the lead and lead compounds pose environmental hazards and must be recycled. Lead batteries may generate hydrogen during over charge-discharge causing pressure build-up and explosion. There are many reported injuries every year due to abuse of lead acid batteries. Concentrated Sulfuric acid is used as the electrolyte in lead-acid battery, and can burn and cause permanent damage

and blindness [2, 3]. Nickel metal hydride batteries are also widely used as rechargeable batteries, where hydrogen storage alloys are used as anode and nickel hydroxide as the cathode. The electrolyte in nickel metal hydride battery is concentrated aqueous solution of potassium hydroxide. The inherent low voltage stability of aqueous electrolytes limits the voltage of this type of cells to the thermodynamic decomposition voltage of water, 1.23 V. This low cell voltage limits the energy density of batteries with aqueous electrolytes. During the last two decades, significant attention is paid to the use of organic based electrolytes in the development of high voltage lithium batteries.

1.4 Lithium Ion Batteries

Lithium ion batteries have attracted much interest in last few years because of their high energy density and potential for lower cost in the future. They are the most popular batteries in portable electronic devices because of their high energy densities and low self-discharge. Unlike lithium primary batteries, which are disposable, lithium-ion batteries use intercalation/ deintercalation lithium compounds as the anode and cathode material. They have many advantages over other type of secondary batteries. They can be made in various shapes and sizes to suite the device applications. They are much lighter than other energy-equivalent secondary batteries. They have high open circuit voltage in comparison to batteries like lead acid or nickel metal hydrides. They have no memory effect. Its self -discharge rate is less than 5-10% per month, compared to over 30% per month in common nickel metal hydride batteries, and 10% per month in nickel cadmium batteries [1].

1.4.1 Cell Components

The basic building block of a battery is the cell, which consists of anode, cathode and electrolyte, schematically shown in Figure 1.2.
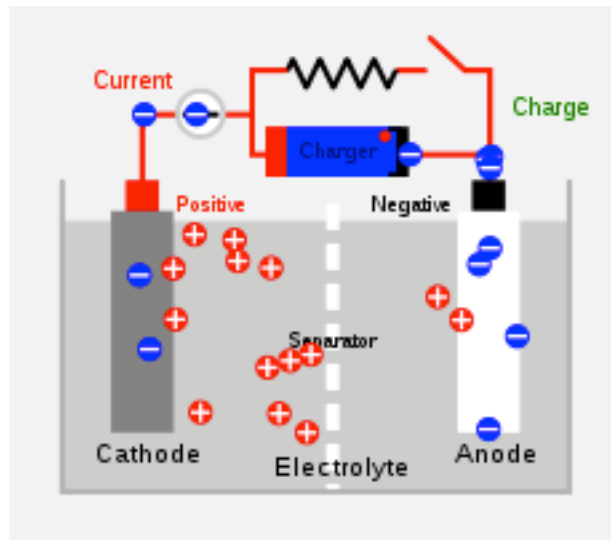
Figure 1.2 Components of a Cell

1.4.1.1 Anode

An anode is the negative electrode from which electrons flow out towards the external circuit during discharge. In order for a material to work as anode, it should easily oxidize to give up electrons. Commonly used anode materials in lithium batteries are lithium alloys, and lithium intercalated carbonaceous materials, which can be easily oxidized. Discharge reaction of a typical anode is represented by the following reaction.

$$LiC_6 \rightarrow Li^+ + e^- + 6C \qquad (1.1)$$

1.4.1.2 Cathode

A cathode captures electrons from the external circuit (during discharge) and hence gets reduced. Thus, for a material to work as cathode, it should easily get reduced i.e. it should have

high electron affinity. Commonly used cathode materials are transition metal oxides. The discharge reaction of a transition metal oxide can be represented as the following reaction.

$$M^{IV}O_2 + Li^+ + e^- \rightarrow LiMo^{III}O_2 \qquad (1.2)$$
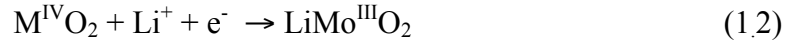
1.4.1.3 Electrolyte

While the electrons are passing through the external circuit during charge-discharge, lithium ions released form one electrode are transported through the electrolyte and inserted into the other electrode to maintain electoneutrality.   In order to sustain the flow of electrons, the newly formed ions have to pass between the electrodes. So there should be a medium to move the ions from one electrode to the other inside the cell: an electrolyte is used for this purpose. Electrolyte should be such that it facilitates the movement of ions. Also it should not conduct electrons. Otherwise the electrons will flow through it and there will be short-circuiting. A separator is used to separate anode and cathode to avoid the short-circuiting. A separator that contains electrolyte is permeable to electrolyte to allow movement of ions.

1.4.2 Fundamentals of operation

Charging/discharging process in lithium ion battery is shown in Figure 1.3. In a typical metal ion battery, metal ions work as a charge carriers. They transport charge from anode to cathode and vice versa as described below. Assume M^{+n} as the metal ion charge carrier, C as a positive electrode (cathode) and A as negative electrode (anode). In the process of charging, M^+ leaves C generating 'n' numbers of electrons that migrate towards A (anode) while electrons travel through external circuit. At anode, metal ion combines with 'n' electron liberated from cathode and gets intercalated into the anode forming AM.

$$MC \leftrightarrow C + M^{-n} + ne$$

$$MC^{III} \rightarrow M^{+n} + ne^- + C^{IV}$$

$$A + M^{-n} + ne \leftrightarrow AM$$

$$A + M^{+n} + ne^- \rightarrow MA$$
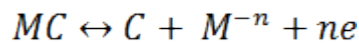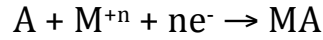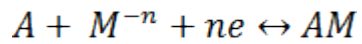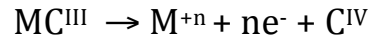
Overall reaction is

$$MC + A \leftrightarrow C + MA \qquad\qquad (1.3)$$

M can be considered as Li, in lithium battery.
Thus it is a reversible reaction in which metal ions are exchanged between anode and cathode (a

shuttle mechanism).
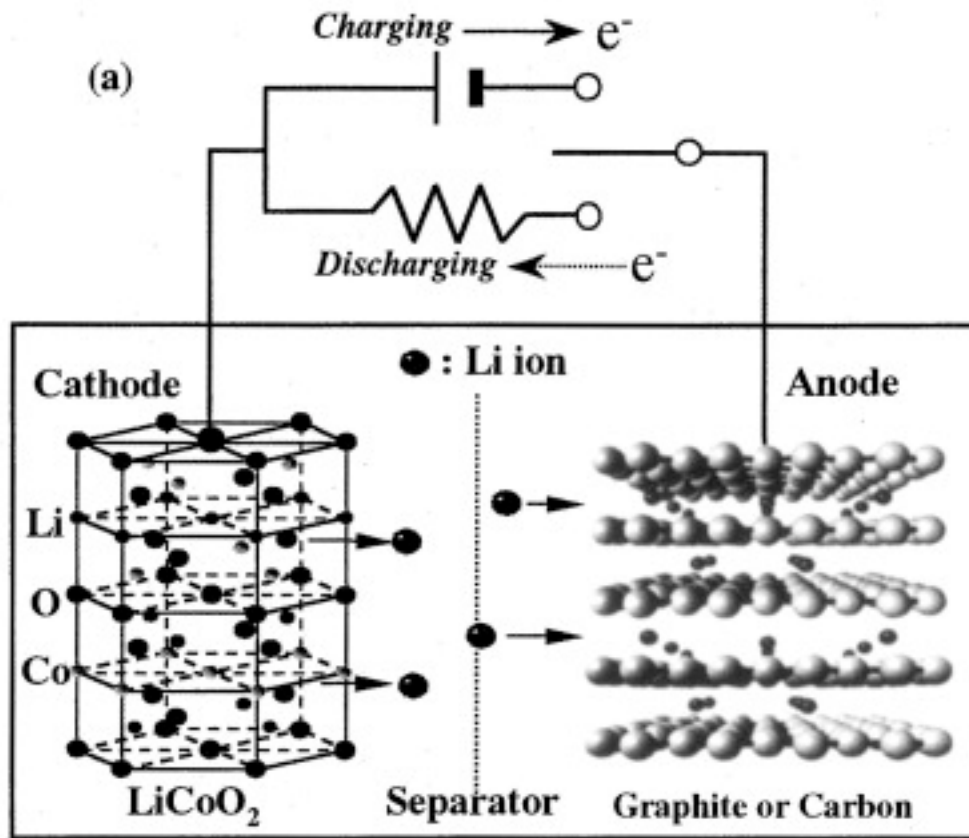
Figure 1.3 Charging- mechanism in Li-ion battery [4]

As there is oxidation and reduction taking place, it is considered as redox reaction. In a

lithium ion battery, the metal is Li. During the charging process, Li-ions will move towards the

negative electrode. So a potential difference will be established between the two electrodes. And during the discharge process, lithium ions will go back to the positive electrode called cathode and hence there will be flow of electrons in the external circuit. All the three major components anode, cathode and electrolyte play important roles in the overall performance of a battery. Electrolyte should have high ionic conductivity to reduce ohmic losses. To avoid the short-circuiting problem, it should be an electrically insulating material. Similarly, there are requirements for anode and cathode parts of the battery. Cathode material plays a major role in deciding the cell voltage because anode material is taken with voltage almost close to the metallic lithium. There are major efforts to develop alternative anodes based on lithium alloys. However, the present work focuses on improving cathode materials.

1.5 Cathode materials

A cathode material should have high Gibbs free energy to provide high redox potential ($E = \Delta G/nF$ where ΔG is the Gibbs free energy, n-number of electron exchange during the reaction, F-Faraday's constant, 96500 A.s), exhibiting a readily reducible/oxidizable redox center, for example a mid- or later- transition metal ions can serve as redox center. The use of non transition metals is also being investigated [5]. The material should be able to react with lithium in a reversible manner (insertion and extraction) and it should have high rate for insertion and extraction during discharging and charging. This will increase the amount of energy transferred per unit time and hence will lead to a high power density. The material should be a good ionic and electronic conductor, to reduce IR drop in the electrode. This allows for the easy addition or removal of electrons and ions during the electrochemical reaction and the reaction to occur uniformly throughout the cathode rather than at the electrode/electrolyte interphase. The material should be stable during multiple charge-discharge cycles with good lattice stability. The cathode

material also should be low cost, particularly for large format cell applications and should be environmentally acceptable. To fulfill all these requirements, three major types of cathode materials have been studied in the past.

1.5.1 Layered Type Oxides

Layered materials are considered as good candidates for cathode in Li ion batteries due to their very high theoretical capacity (e.g. $LiCoO_2$ capacity is ~ 275 mAh/g). This material consists of layers of lithium ion and transition metal oxide (MO_6 octahedral) linked through corner-edge-face sharing, , which facilitates lithiation and delithiation as shown in Figure 1.4. Despite very high theoretical capacity, experiments have shown that it is not possible to achieve this value [6].
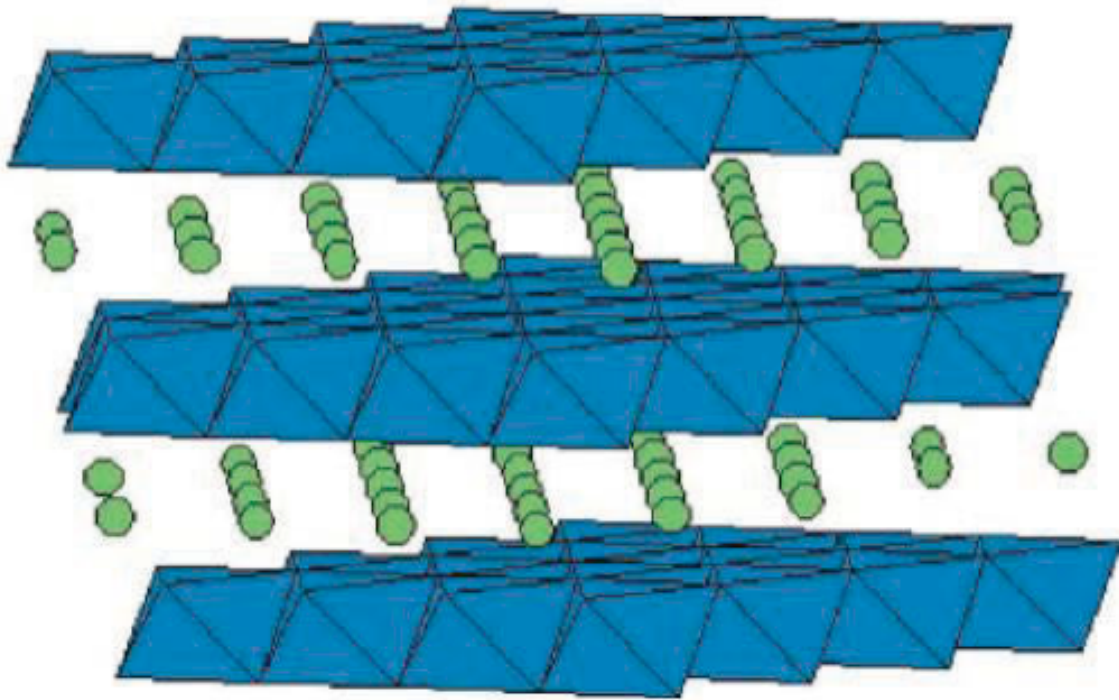
Figure 1.4 Layered type oxides

The maximum practical capacity that can be achieved is about half of the theoretical

capacity value ($LiCoO_2 \leftrightarrow 1/2Li^+ + 1/2e^- + Li_{1/2}CoO_2$). This is due to strong repulsion of MO_6 layers with negatively charged oxygen facing each other, and anisotropy in the structure of these materials during lithiation process [7]. For instance, in $LiCoO_2$, a transition from hexagonal to monoclinic crystallographic phase occurs when half of lithium goes out of the material, resulting in 3% volume expansion leading to a significant reduction of capacity [5, 8]. As these materials are made of alternate layers of lithium and transition metal oxide, taking all the lithium out may result in ion-mixing and collapse of the lattice structure. In addition, the lithiated transition metal oxides may decompose exothermally at high state of charge and generate oxygen and extreme heat.

1.5.2 Three-Dimensional Spinel oxides

The spinel structure named after mineral $MgAl_2O_4$ with the general formula AB_2O_4 is shown in Figure 1.5. It is essentially cubic, with O^- ions forming a close packed fcc lattice.

Oxygen

B-atoms octahedral sites

A-atoms tetrahedral sites

AB_2O_4 spinel The red cubes are also contained in the back half of the unit cell
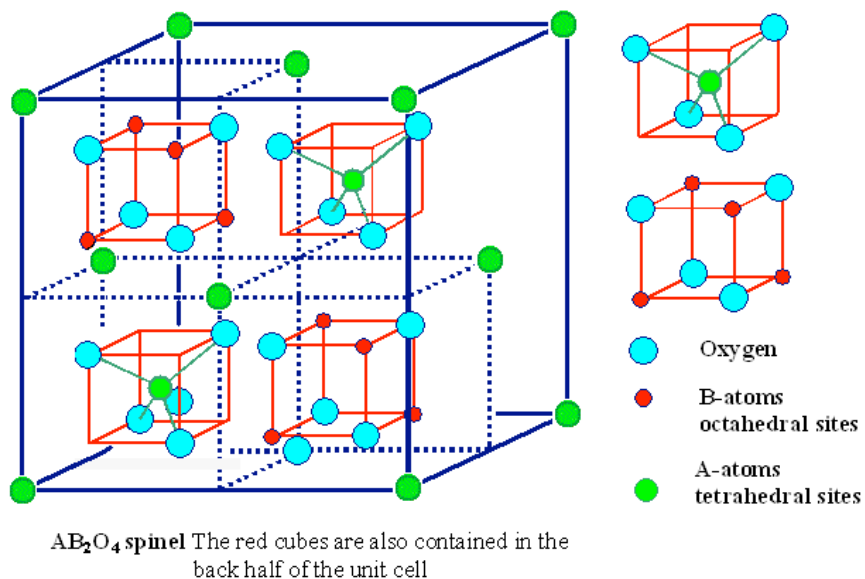
Figure 1.5 Spinel structure [9]

The cations occupy 1/8 of the tetrahedral sites and 1/2 of the octahedral sites with 32 O ions in each unit cell. $LiMn_2O_4$ is a good spinel cathode material to use as electrode in Li-ion batteries, which has a charge storage capacity of 148 mAh/g [10, 11]. It has the advantages of low-cost, environmental friendliness, and high abundance. But problem with spinel based battery material is that its capacity fades with cycling, particularly, above 45 °C, due to the dissolution of manganese ion and the Jahn-Teller distortion associated with the Mn^{III} ions.

1.5.3 Polyanions

Polyanions are promising materials introduced by Goodenough in 1990s [12]. General formula is $Li_xM_y(XO_4)_z$, where X is one of P, S, As, Mo, or W and M is the transition metal. One of the most studied polyanions is $LiFePO_4$. Lithium iron phosphate has been investigated and considered as one of the most promising material due to its high theoretical capacity value (170 mAh/g), low cost, reversible charge-discharge cyclic stability and thermal stability [13, 14]. Thermal stability is a very important safety feature for the use of these batteries in electric vehicles.

$LiFePO_4$ has an orthorhombic olivine structure, with space group *Pnma*, combined with PO_4 tetrahedra, corner-sharing FeO_6 octahedra, and edge sharing LiO_6 octahedra.
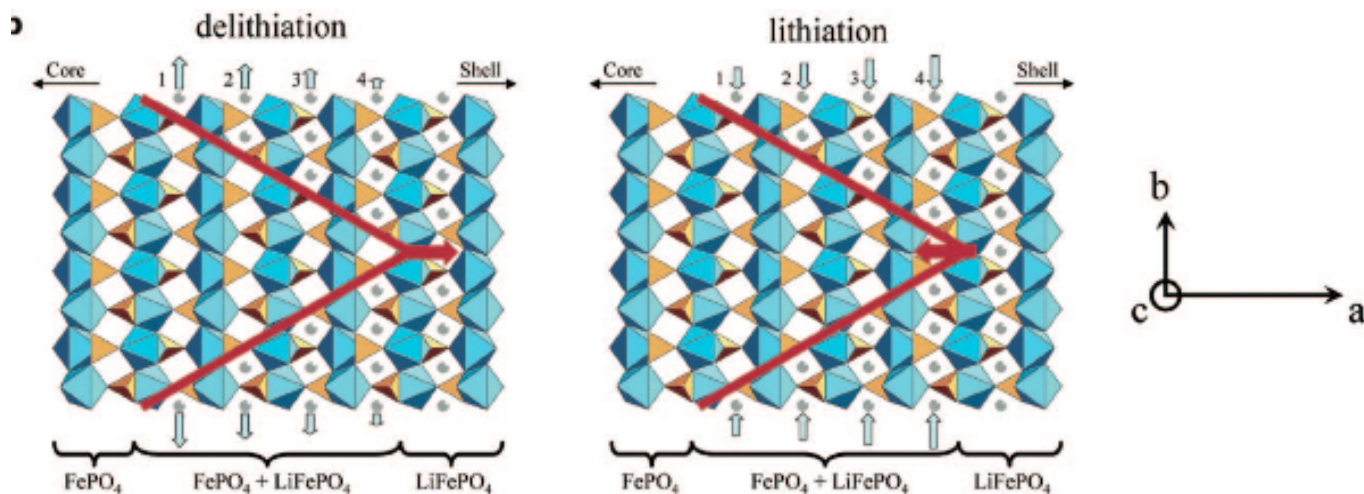
Figure 1.6 FePO$_4$/ LiFePO$_4$ lithiation and delithiation process [15]

The material is structurally very stable, due to strong P-O covalent bond. Even when all the Li-ions are removed, it retains its olivine structure. Thus there is no significant distortion in the structure during the insertion or extraction of lithium ions. During the lithium extraction LiFePO$_4$ is converted into FePO$_4$, which has a similar structure as that of LiFePO$_4$. Figure 1.6 shows the structure of FePO$_4$ and LiFePO$_4$ during the lithiation – delithiation process. There is experimental evidence showing FePO$_4$/LiFePO$_4$ to be biphasic material during insertion/extraction of lithium ions [16].

The main reason why it took so many years to switch from research to development of this product is its low intrinsic electronic conductivity ($\sim 10^{-9}$ S cm^{-1}) and very large particle size. Due to their very poor conductivity, initial reports indicated that Li-ion can only be partially extracted/inserted at room temperature at modest rates. At high temperature (i.e. 60°C), the reversible capacity of LiFePO$_4$ was significantly improved [14]. Armand et al. were the first to show that by coating an electronically conducting layer on LiFePO$_4$, almost full theoretical

capacity could be achieved at 80°C using a polymer electrolyte cell [17] . However, improving the electronic conductivity and getting smaller particle size to achieve best results at room temperature is still a matter of great interest. Different new methodologies of materials preparation have been used to compensate for these apparent drawbacks, such as freeze-drying methods [18] and spray pyrolysis [19]. Many modifications including heterogeneous doping by metal ions, coating with an electron-conducting phase (mostly carbon) and particle size minimization have also been investigated [20-22].

1.6 Motivation and Scope of the Thesis

$LiFePO_4$ is a potential candidate for cathode in Li ion batteries but its very low electronic conductivity prohibits its use in Li ion batteries. As discussed earlier, various techniques have been developed to overcome this limitation. Although, capacity close to theoretical value at low rate has been reported using various methods [18, 23, 24], high rate capability of $LiFePO_4$ still remains a challenge. It shows better performance at very small applied currents, but its capacity deteriorates considerably at large applied currents [25]. The objective of this thesis is to improve electrochemical performance of $LiFePO_4$ at higher applied currents.

We prepared $LiFePO_4$ by a simple sol gel method and used different techniques to improve the electronic conductivity and hence electrochemical performance. The summary of the research is as follows

(1) Coating with carbon has become a traditional method to improve the performance of $LiFePO_4$. However, very thick coating of carbon on $LiFePO_4$ can affect the electrode/electrolyte interface. As graphene is known for its high electron mobility, we prepared $LiFePO_4$/graphene oxide composite using sol gel method followed by calcination at 600°C. We found that addition of graphene improved the electronic

conductivity by 6 orders of magnitude and prepared electrode was stable at very high charging/discharging rate.

(2) Secondly, we studied the effect of temperature dependent impurities in $LiFePO_4$ by annealing the samples at various temperatures. We found that annealing $LiFePO_4$ for long time yields Fe_2P and Li_3PO_4 impurity phases, which grow with increasing annealing temperature. Fe_2P is known to be a very good electronic conductor. But excess amount of Fe_2P will result in poor performance as Fe_2P grows at the cost of active $LiFePO_4$. Our results have shown that annealing at 700ºC yields optimum amount of Fe_2P for best electrochemical performance compared to samples annealed at 600ºC, 800ºC and 900ºC.

(3) We have also studied the effects of doping indium at Fe site in $LiFePO_4$. We found that adding indium enhances the capacity values of $LiFePO_4$. Following the study done in our research group, which found that 1% In doping gives best results, we studied 1% doped samples at different annealing temperatures and found that the samples annealed at 700ºC delivers best the electrochemical performance. We also compared the indium doped samples with samples without doping and demonstrated that doping with indium yields better electrochemical results.

CHAPTER 2

EXPERIMENTAL DETAILS

2.1 Synthesis Method

There are many different established methods to prepare $LiFePO_4$, namely solid state, hydrothermal, microwave synthesis, polyol, sol-gel etc. We used simple sol-gel method to synthesize $LiFePO_4$. Sol-gel is a method in which precursors are dissolved in a solvent and subsequently allowed to mix together in a flask. Some materials can be synthesized in open air while others require special environment to avoid unwanted side products in the final sample. $LiFePO_4$, preparation should be under inert atmosphere as iron has the tendency to get oxidized easily in air and hence reaction usually is carried out under the flow of nitrogen or argon.

This method has been used extensively to form $LiFePO_4$. Back in 2002, F. Crose *et al* [26] prepared $LiFePO_4$ by sol-gel using $LiOH$, $Fe(NO_3)_3$ and H_3PO_4 as precursors. An interesting point in this synthesis was that the reaction was allowed to occur in air. They claim that H_3PO_4 was acting as reducing agent and was reducing Fe^{+3} to Fe^{+2} simultaneously. Metals such as copper and silver were used to provide a conducting network. They observed a capacity value of 145 mAh/g at very low rate of C/5, which dropped down to 100 mAh/g when discharged at 1C rate. M. Doeff *et al* [27] compared the solid-state reaction with sol-gel method for preparing $LiFePO_4$ and found that $LiFePO_4$ prepared by sol-gel method yields more sp2 carbon, which is a better conductor than disordered sp3 carbon. Out of a series of samples synthesized, $LiFePO_4$ processed with naphthalenetetracarboxylic dianhydride showed the best capacity of 126mAh/g at 0.055 mA/cm^2. Y Hu *et al* [28] reported another comparison study. They synthesized $LiFePO_4$

with sol-gel method and used Mg and Ti as dopant on the lithium site. For comparison $LiFePO_4$ was also prepared by solid state method. In solid state reaction, $LiOH$, $Fe(CH_3COO)_2H_2O$ and $NH_4H_2PO_4$ were mixed and ball milled in acetone followed by heating at $300^{\circ}C$. . The powder obtained was annealed at $600^{\circ}C$ for 8 Hrs under flow of nitrogen. For the sol-gel process $Fe(NO_3)_3$, $Li(CH_3COO)$, H_3PO_4 and $OHCH_2COOH$ were used as precursors. Doping was achieved by using 1% mol of $Mg(NO_3)_2 \bullet 6H_2O$ and $Ti(OCH_2CH_3)$ maintaining the pH of the mixture solution between 8.5 and 9.5 by using ammonium hydroxide. A gel was obtained under the nitrogen flow at $90^{\circ}C$ followed by heating at $500^{\circ}C$ under nitrogen. The resulting powders were annealed to $600^{\circ}C$ or $700^{\circ}C$ for different times. They found that sample prepared by solid-state method showed the best capacity value, as the annealing temperature was lower than sol-gel prepared samples. J Yang et al [29] synthesized 200-300 nm particles with a uniform size distribution using sol-gel method. They dissolved lithium acetate, iron acetate and phosphoric acid in ethylene glycol and let it mix thoroughly by subsequent heating at $700^{\circ}C$ for 10 hours to yield the carbon coated $LiFePO_4$ particles. They found that 0.75M ethylene glycol sample exhibited almost theoretical capacity at very low rate of C/100. At rates of C/5 and 2C capacity obtained was 150 mAh/g and 140 mAh/g.

In our studies, we prepared $LiFePO_4$ using lithium acetate, iron chloride and phosphorus pentoxide as precursors. Desirable amount of these materials were dissolved in 200 proof ethanol inside a three-neck flask. The solution was kept under vigorous stirring under the flow of N_2 for three hours, then a carbon source dissolved in ethanol was added to the solution and the resulting mixture was further allowed to mix for three hours. Finally, the solution was put on a hot plate at $80^{\circ}C$ to get a dried powder, which was further annealed at higher temperatures to obtain the final product.

2.2 Characterization Techniques

2.2.1 X-ray diffraction

Powder x-ray diffraction is a commonly used technique to determine the crystallinity of various phases present in the sample. It uses X-rays of shorter wavelength (0.01-10nm), which is comparable with the size of interatomic distance in the crystal. Most commonly used x-ray sources are Cu and Mo which produce x-rays of wavelength 1.5418 and 0.8 A. Arrangement of atoms in different planes in a crystal causes diffraction of x-rays as they pass through the crystal. The condition for diffraction is defined by the Brag's law

$$2d_{hkl}\sin\theta_{hkl} = n\lambda \qquad\qquad (2.1)$$

where n is an integer, λ is the wavelength of the incident X-rays, θ_{hkl} is the angle between incident beam and crystal plane and 'd' is the inter planar distance. h,k,l are called Miller indices and they define hkl a unique set of crystal planes in the crystal. Using the width of a diffracted peak at half maximum, crystallite size can be estimated using Debye –Sherrer equation

$$FWHM = K\lambda/D\cos\theta \qquad\qquad (2.2)$$

where FWHM is full width at half maxima of the peak corresponding to 2θ. 'K' is taken as a constant that includes instrument broadening and lattice category and λ has value 1.54 Å. Usually 'D' is calculated for multiple peaks and average is considered as the crystallite size.

In this study we used a Rigaku Miniflex 600 x-ray diffractometer with, Cu k-α radiation (wavelength 1.54 Å). It is a stationary source, rotating stage and detector arrangement

instrument. A 40 kV voltage and 15mA current was used to acquire the spectrum at the rate of 1degree per min.

2.2.2 Scanning Electron Microscopy

Scanning electron microscopy is a tool to explore the surface morphology of a material as well as the elemental analysis. It uses electrons for imaging, which are generated in an electron gun maintained at high vacuum. Once these energized electrons hit the sample, they produce many signals including secondary electrons, backscattered electrons and x-rays. For the imaging purpose, secondary electrons are detected by detector. These electrons are used to produce the final image on screen. X-rays produced at the sample can be used to do the elemental analysis. For our studies we used JSM-6510 LV-LGS SEM at voltages between 15kV to 30kV to look at the morphology and particle size of our samples.

2.2.3 Transmission Electron Microscopy

Transmission electron microscope is based on the same principle as the light microscope. Light microscope uses photons to image a sample whereas TEM uses electrons for this purpose. As it is clear that spatial resolution is directly proportional to the wavelength of the radiations used, TEM has much higher resolution than light microscope as it uses electrons, which exhibits much lower wavelength as compared to photons. TEM can image thousand times smaller object than a light microscope. Electron are generated in an electron gun and then focused by electromagnetic lenses towards the specimen. Unlike SEM, TEM uses transmitted electrons for imaging. For our studies we used JOEL-2010 at a voltage 200kV.

2.2.4 Raman Spectroscopy

Raman spectroscopy is based on interaction of incident photons with the molecules of a material. When photons are incident on a material, they can either be absorbed or can be scattered. Further in scattering, there are three possibilities: (1) If the scattered photon has same energy as incident photon, scattering is called Rayleigh scattering (2) if the scattered photon has energy lower than the incident photon energy, it is called Stokes Raman Scattering (3) If the scattered photon has energy higher than the incident photons, it is called Anti-Stokes Raman scattering. The change in energy of the scattered photons is equal to the vibrational energy of the atoms in a molecule/crystal. Raman shift is given by following equation

$$\Delta \bar{v} = 1/\lambda_{incident} - 1/\lambda_{scattered} \qquad (2.3)$$

where $\Delta \bar{v}$ is change in wavenumber with units of cm^{-1}.

We used a Jobin-Yvon Horiba Triax 550 spectrometer for collecting Raman Spectra. The system is equipped with liquid nitrogen cooled charge coupled detector, an Olympus BX41 microscope with 10X, 50X and 100X objective lenses and Argon-ion 514.5nm laser. The scattered signal was collected through the same objective and was focused on the entrance slit of a spectrometer with a 1200 lines/mm diffraction grating. Rayleigh scattered photons were blocked by a notch filter near the entrance slit.

2.2.5 Magnetic Measurements

Magnetic measurements were carried out with a Physical Properties Measurement System (PPMS). PPMS is capable of performing many different kinds of measurements like AC and DC magnetization, specific heat, dielectric constant in temperature range of few Kelvin to room

temperature. A high magnetic field of 8T can be applied. We used PPMS to confirm various magnetic phases in our samples. We performed temperature dependent ac magnetization measurements to find out the transition temperatures. We also measured saturation magnetization (M) by varying the magnetic field (H) from -5T to +5T.

2.2.6 X-ray Photoelectron Spectroscopy

X-ray photoelectron spectroscopy is a powerful technique to find out the electronic state of the atoms as well as ionization energy of electrons in atoms. When x-rays of known energy strike the sample surface, orbital electrons absorb energy and   get emitted out of the orbit with kinetic energy. Energy analyzer measures kinetic energy of emitted photoelectrons. According to law of conservation of energy

$$h\nu = B.E. + E_k \qquad\qquad (2.4)$$

Where $h\nu$ is energy of the incident x-rays and E_k is kinetic energy of the electron.

So, binding energy can be calculated from incident x-ray energy and kinetic energy of emitted electrons. Binding energy for electrons in the various shells is different as they experience different nuclear force. So by selecting an element of interest from specimen, one can get various binding energy levels for the element, which corresponds to the oxidation state of that element. .

In one of our studies, we used XPS to characterize carbon present in our sample. We used Perkin-Elmer's system, which is equipped with Al Kα (1486.6eV) x-ray source. A pellet made under vey high pressure was kept in the chamber at 10^{-9} torr.

2.2.7 Mössbauer Spectroscopy

Mössbauer spectroscopy is a powerful tool to observe the local electronic structure around the nucleus of an atom/ion in the sample. It is based on Mössbauer effect discovered by Rudolf Mössbauer in 1957. In a free nucleus, taking into account for the conservation of momentum, nucleus should recoil when emission or absorption of gamma ray occurs. So during absorption, energy of the gamma ray should be little more than the difference of energy levels and vice versa. It is very difficult to achieve resonance for a free nucleus. Mössbauer found that this could be addressed by fixing the nucleus. In solids, some of the nuclei are not free to move. So using these nuclei, nuclear resonance spectroscopy can be performed. Many energy level transitions occur when a gamma ray is absorbed or emitted by nucleus. These transitions depend upon the electronic and magnetic environment around the nucleus, which means magnetic impurities in a sample can be studied by Mössbauer spectroscopy. Mössbauer spectroscopy can be done only on stable isotopes of elements and the source for studying a particular isotope has to be chosen so that it decays into isotope under study after emitting gamma ray. ^{57}Fe and ^{57}Co make such a pair. There are three main parameters which are used in analysis of a Mossbauer spectroscopy (1) Isomer shift (IS) (2) Quadrupole splitting (QS) and (3) Hyperfine splitting (HS). IS is a measure describing a shift in resonance energy of nucleus due to the local electronic structure around the nucleus. So it can give information about the valance state of an element say Fe. In a typical Mössbauer spectrum, it appears as shift from zero velocity (Figure 2.1). QS splitting results from asymmetric distribution of charge around the nucleus. Due to this asymmetry, nuclear quadrupole moment interacts with electric field due to asymmetric charge distribution. In case of iron I=3/2 splits into I=+3/2 and I =-3/2. As shown in figure 2.1 QS is measured as the difference between two dips. HS is caused by the interaction of the nuclear magnetic moment with the

ferri/ferromagnetic material's magnetic field. This interaction results in splitting of nuclear energy levels, which can be observed as six peak pattern in a Mossbauer spectrum (Figure 2.1).

In our studies, we used Mossbauer spectroscopy to investigate the valance state of Fe. Fitting the data with MossFit gave the IS and QS values and those values were used to infer the oxidation state of iron.
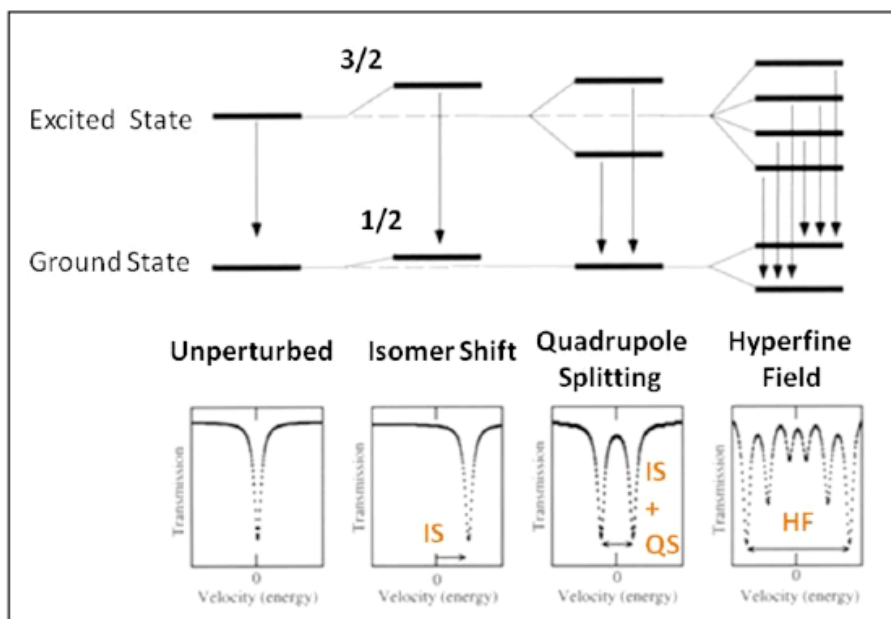
Figure 2.1 A typical Mossbauer parameter spectra [30]

2.3 Fabrication of electrochemical cell and electrochemical measurements

The electrochemical characterization of the samples was performed using standard coin cell geometry with lithium metal as an active anode. The active cathode materials and Super P as a conducting material were mixed (95:5 ratio) and ground for 20 min (without the use of

conventional binder-Polyvinylidene Floride). The homogenous mixture was then put on an aluminum mesh and pressed between two steel cylinders. The aluminum mesh acts as a current collector. It is advantageous to test intrinsic property of active electrode materials without the contribution of binders. There are many fundamental studies on cathode materials without the use of binders, such as single particle electrochemistry [31], solid-state pellets for in situ work [32, 33] and thin film produced by sputtering [34]. One advantage of testing cathode materials without binder is that the effect and contributions of the binder on electrochemical property of the materials are eliminated. The prepared cathode was cycled against Li metal electrode as a counter electrode separated by a polymeric separator soaked in a binary electrolyte consisting of ethylene carbonate (EC) and dimethyl carbonate (DMC), (50:50) containing 1M LiPF$_6$. The room temperature galvanostatic charge and discharge measurements were carried out at different C-rates in the voltage range 2.2 – 4.2 V.

2.3.1 Electrochemical Impedance Spectroscopy (EIS)

In an ideal resistor, resistance is defined as its ability to provide hindrance to flow of current through it. But in complete circuits, there are other elements like capacitor and inductor and hence overall hindrance to current passage depends on all these components. For these kinds of circuits, frequency dependent term impedance (Z) is used. EIS studies the current response of a system to the applied sinusoidal ac signal of varying frequencies. Impedance has real (Z$_{real}$) as well as imaginary components (Z$_{img}$) as seen in the following equation

$$Z = Z_o \left(Cos\Phi + jSin\Phi \right) \qquad (2.5)$$

If $-Z_{img}$ is plotted vs Z_{real}, the plot is called a Nyquist plot and modeled with Randal's circuit for a Li ion cell (Figure 2.2(a) and (b)). Equivalent Randel's circuit consists of solution resistance (R_s) which corresponds to resistance imposed by the electrolyte, charge transfer resistance (R_{ct}) – the resistance faced by an electron at the interface of electrolyte and electrode and Warburg resistance (R_w)-related to ionic diffusion through the electrode. Another component of the circuit is constant phase element (CPE) which corresponds to the double layer capacitance contribution. Although, frequency values can not seen directly in the plot, different parts of the curve can be assigned as different frequency regions.
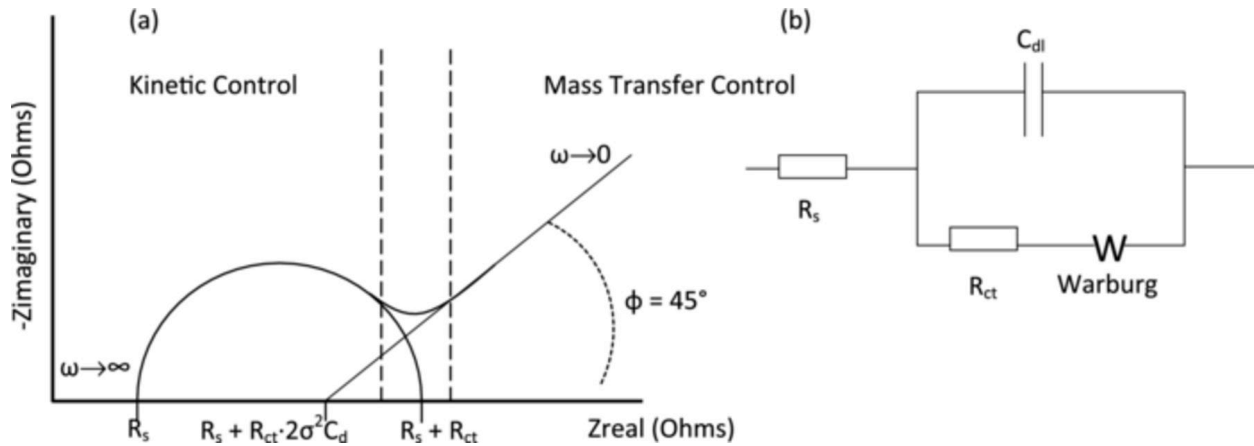
Figure 2.2 (a) Nyquist Plot (b) Equivalent Circuit for an electrochemical cell [35]

A typical Nyquist curve for a Li ion cell can be described in three different regions. (1) Part of the curve up to R_s is high frequency region, where diffusion of Li ion through electrolyte is measured. (2) The mid frequency range measures the charge transfer and represented by the semicircle (3) The low frequency region, called Warburg region, gives information about mass transfer i.e. Li ion diffusion.

2.3.2 Cyclic Voltammetry

Cyclic voltammetry (CV) is an electrochemical technique in which current produced due to Redox reaction is recorded as a function of potential applied.
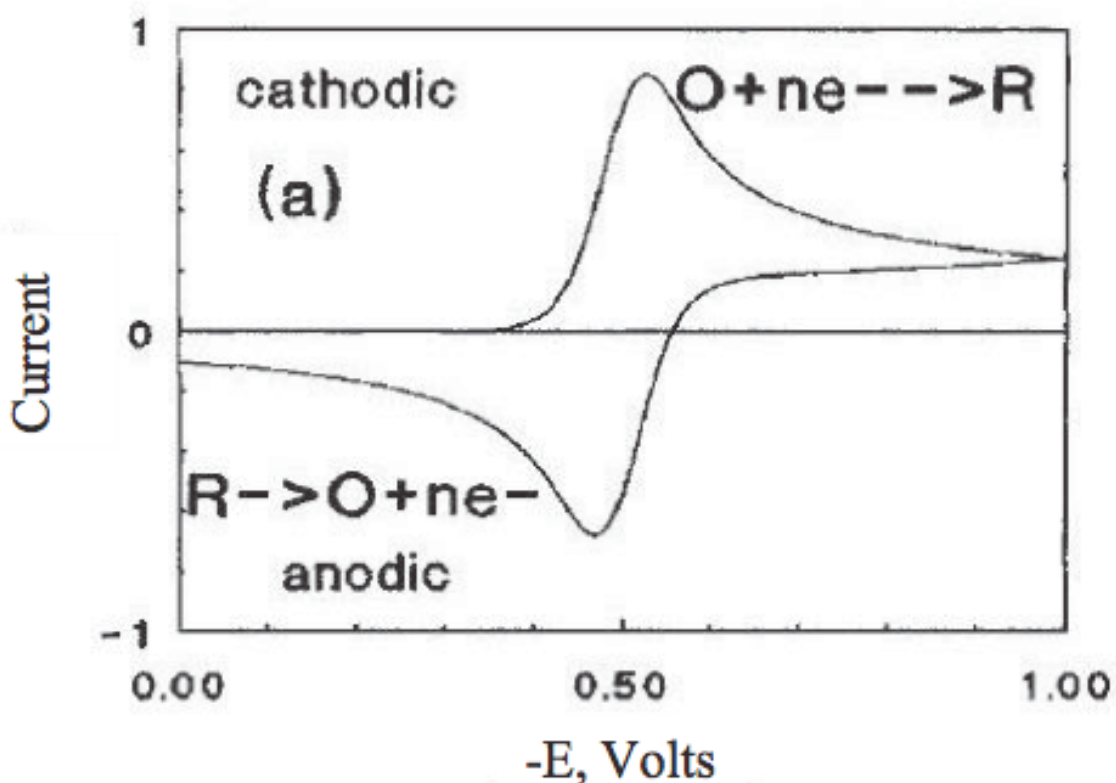
Figure 2.3 Cyclic Voltammogram [36]

CV is usually carried out in certain potential range depending on the material being analyzed as the potential is swept linearly with time.

During the potential sweep up, depending upon the characteristic of material, it will go through oxidation or lose an electron at certain value of potential, which in turn gives out positive current, and a peak appears at that potential value due to the mass transfer limitation to the electrode. Once the potential hits the highest assigned value (upper voltage limit), the voltage

is swept back to the lowest set potential (lower voltage limit) and the reduction peak appears with negative maximum current value (Figure 2.3).

Cyclic voltammetry is not just for finding about the oxidation/reduction peaks but also for revealing the kinetics of the electron transfer and mass transport during an electrochemical reactions. Li ion diffusion coefficient can be obtained from the Randles-Sevcik equation shown below

$$\mathbf{i_p = 0.4463\ n\ F\ A\ C\ (n\ F\ v\ D\ /\ R\ T)^{1/2}} \qquad (2.6)$$

where, n is the number of electrons exchange for the reaction, **v** is the scan rate (V / sec), **F** is the Faraday's constant (96485 C / mol), **A** is the electrode area (cm^2), **R** is the universal gas constant (8.314 J / mol K), **T** is the absolute temperature (K), and **D** is the analyte's diffusion coefficient (cm^2/sec). Slope of graph between peak current and square root of scan rate is Li-ion diffusion coefficient. Cyclic Voltammetery measurement was carried out using PHE600 Gamry Electrochemical System in range of 2.5V to 4.2V.

2.3.3 Constant current charge-discharge

Constant current charge-discharge is a technique of electrochemical measurements, in which a constant current is applied to the cell and voltage is recorded as a function of time. While performing this measurement, current is set to reverse once highest assigned voltage is reached, which gives information on the charging and discharging curves together. These measurements can be done on various rates depending upon the constant current applied. Time taken to complete a single charge/discharge is used to find out the C rate for the measurement, which is inversely proportional to the amount of time (hours) it takes to complete a charge of

discharge cycle. If charging/discharging takes one hour, C-rate is defined as rate of 1C, and if it take 2 hours, it is C/2 rate, etc. The main purpose of this measurement is to find out capacity of the materials in mAh/g. Cyclic voltammetry results can be used to set the voltage range in charging/discharging evaluation. In charging/discharging process of the biphasic samples, there is a plateau at the threshold of the second phase formation. In our samples, this corresponds to the oxidation voltage of the smaple ($LiFePO_4$). The voltage plateau continues till the transformation of first phase to the second phase exists. The length of the plateau is considered as the capacity of the electrode.

CHAPTER 3

ENHANCED ELECTROCHEMICAL PERFORMANCE OF GRAPHENE MODIFIED LiFePO₄ CHATHODE MATERIAL FOR LITHIUM ION BATTERIES

3.1 Introduction

As discussed in Chapter 1, LiFePO₄, initially introduced as a cathode material for Li ion batteries by Goodenough's group, and has been investigated extensively in the past few years mainly due to its reasonably high theoretical capacity (170 mAh/g), low toxicity, relatively low manufacturing cost [37], and very good thermal stability [38]. However, prohibitively low electronic conductivity (~10^{-9} S/cm) of LiFePO₄ leads to high impedance, low capacity and low rate capability [39]. Many methods, including carbon coating [40-43], particle size reduction [44-46], and metal doping [21, 47, 48], have been developed to improve the conductivity and capacity of this material. Carbon coating has particularly attracted much interest due to abundance of carbon sources. Many carbon sources such as sucrose [49], carbonaceous polymers [50], carbon rich precursors [51], have been used in the past to coat LiFePO₄ particles or coat LiFePO₄ on vapor grown carbon fibers [52] and carbon nanotubes [53]. Promising results have been reported with the capacity approaching the theoretical value of 170 mAh/g at relatively low charge-discharge rates. However, the deterioration in capacity with cycle life and intolerance to high currents remains a problem that hinders the application of LiFePO₄ in Li-ion batteries for electric vehicles or hybrid electric vehicles, where very high rate capability and cycling stability are required.

3.2 Graphene

Graphene has attracted much attention in all areas of materials science after it was first isolated in 2004 [54]. Graphene has two dimensional nanostructures with outstanding electronic and mechanical properties as well as high surface area [55]. Graphene is a freestanding 2D crystalline layer with one atom thickness of carbon. These carbon atoms are sp^2 hybridized and are arranged in a honeycombed ring, which is considered the fundamental foundation of fullerenes, carbon nanotubes and graphite. One of the most important applications of graphene is its use in composite electrodes for Li ion batteries [56-59]. The graphene composites have been shown to improve the electrochemical performance of $LiFePO_4$ cathode materials because it facilitates electron transfer between the electrode matrix and the $LiFePO_4$ particles, which reduces the internal resistance of the battery and enhances the output power [60-64]. In addition, due to the excellent mechanical property of the graphene, it provides structural stability and improved cyclability to the battery materials.

Ding et al first reported $LiFePO_4$ –graphene composite with a specific capacity of 160 mAh/g compared to 113 mAh/g for $LiFePO_4$ [65]. Su et al introduced graphene into $LiFePO_4$ as a planar conductive additive to prepare a flexible graphene based conductive network [66]. With much lower fraction of graphene additive than those of the commercial carbon based additives, the authors reported better charge discharge performance compared to the commercial ones. L. Wang et al prepared conducting $LiFePO_4$-graphene composite by a facile hydrothermal route followed by heat treatment and found $LiFePO_4$ particles adhered to the surface of the graphene and/or embedded in the graphene nanosheets [56]. The composite that had the composition of $LiFePO_4$ and graphene in the ratio of 92:8, showed a discharge capacity of 160.3 mAh/g at 0.1C and 81.5 mAh/g at 10C due to an improved 3D conducting network bridging graphene

nanosheets. Y. Wang et al prepared LiFePO$_4$-graphene composite by solid-state route and reported specific capacity of 161 mAh/g at 0.1C and 50 mAh/g at 50C [67].

To further improve the electronic conductivity of the composites, 3D porous LiFePO$_4$-graphene composites were synthesized by sol-gel [68] and mechanical mixing methods [69]. In these studies, the capacity values at high rate (10C) were 45-60 and 75 -109 mAh/g without and with graphene, respectively. It appears that composite prepared through sol-gel method shows better capacity at higher rates in comparison to the one prepared by mechanical mixing. Bi et al used three types of strategies, namely, chemical vapor deposition (CVD), Wurtz type reaction (a three step mechanism-first step is to get Cl out of CCl$_4$ and then coupling and assembly of –C=C-layers), and chemical exfoliation to prepare graphene [70]. The authors studied electrochemical performances LiFePO$_4$ with three different graphene samples and claimed that addition of 5% graphene reduced the contact resistance between LiFePO$_4$ particles and improved the overall electronic conductivity of the electrode and hence electrochemical performance of LiFePO$_4$. The authors found that the LifePO$_4$ with graphene prepared by CVD is more effective and produces the capacity values of 132 mAhr/g and 80 mAh/g at 1C and 20C discharge rates, respectively. Most Recently, Hu et al, prepared carbon coated LiFePO$_4$ with surface modification with 2% electrochemically exfoliated graphene [71]. According to the report, they were able to get a capacity value of 208 mAh/g, which is even higher than theoretical value of capacity for LiFePO$_4$. Authors claim that the excess capacity is due to reverse oxidation-reduction between graphene flakes and lithium ions from the electrolyte. From the discussion it is clear that cyclic stability at a particular rate still needs improve. Although Zhou et al. presented a great improvement in the capacity as well as cyclic stability using a spray drying method [57], but their study did not address the critical issue of how the electrical conductivity impacts

electrochemical performance of the cathode material, while the present study establishes a strong correlation between the increase in conductivity and the improved electrochemical performance of the $LiFePO_4$/graphene composite. Since large quantity of graphene oxide can be produced at a relatively low cost compared to graphene, it is important to study the effects of using graphene oxide, as opposed to graphene, as a precursor on the morphology and particle size and consequently the electrochemical properties of the $LiFePO_4$ /graphene nanocomposites. The graphene oxide surface is also more compatible with the $LiFePO_4$, compared to the hydrophobic graphene surface.

In this Chapter, we present the synthesis and characterization of $LiFePO_4$/graphene composite using a simple and cost effective sol-gel method. We demonstrate that the addition of graphene substantially improves the capacity, rate capability and cyclic stability of $LiFePO_4$ without having to reduce significantly the average particle size of $LiFePO_4$. These marked improvements can be attributed to the relatively high conductivity, extremely high surface to volume ratio and good structural flexibility of graphene. As the single layer and few layer graphene sheets make intimate contact with $LiFePO_4$ particles and form a three-dimensional network in the $LiFePO_4$/graphene composite, the conductivity of the composite drastically increases leading to a remarkable improvement in its electrochemical properties evidenced by a dramatic increase in the capacity from 60 mAh/g for $LiFePO_4$ to 160 mAh/g for $LiFePO_4$/graphene nanocomposite at C/3 rate. We used graphene oxide as precursor for the synthesis of $LiFePO_4$/graphene and finally converted it to graphene during sample annealing. The presence of graphene was confirmed by Raman spectroscopy and XPS. In addition, our method did not show any residual oxygen in the final graphene product in contrast to the other methods [57].

3.3 Preparation of LiFePO$_4$ and LiFePO$_4$/graphene

LiFePO$_4$ (LFP) was prepared by sol-gel method using lithium acetate dihydrate, 99% (Alfa Aesar), ferrous chloride (Fisher Scientific), and phosphorous pentoxide (Fisher Scientific) as precursors. Ferrous chloride and phosphorus pentoxide were dissolved in 200 proof ethanol, mixed and stirred for 3 hours in nitrogen atmosphere. Then the lithium acetate, also dissolved in 200 proof ethanol, was added to the solution and allowed to mix for another 3 hours under-nitrogen atmosphere. To prepare LiFePO$_4$/graphene (LFP/G) composite, a highly concentrated graphene oxide aqueous dispersion (0.5% by weight) was diluted with ample amount of ethanol and subsequently added to the mixture following the addition of lithium acetate. This mixture was allowed to mix for an additional 3 hours and then the sample was dried at $85\,^{o}C$. Both LFP and LFP/G samples were heated at 200 ^{o}C for 2 hours in vacuum to remove the moisture, and subsequently annealed at 600 ^{o}C for 5 hours with a constant flow of forming gas (90% Ar and 10% H$_2$) to simultaneously form a phase pure LFP and reduce graphene oxide to graphene (in LFP/G). The weight ratio of GO to LFP was 1:9 (or 10% of GO).

3.4 Results and Discussion

Figure 3.1 shows the XRD patterns of LFP samples with and without graphene. For both samples, all the Bragg peaks can be indexed to the olivine structure of LFP phase with an orthorhombic system and space group of *Pnma*, suggesting that the samples do not contain any crystalline impurity phases within the detection limit of XRD. The absence of any XRD peaks from graphene suggests that the graphene sheets in the LFP/G composite are randomly oriented and homogeneously distributed. The average particle size was determined to be ~ 50 nm, in both the samples using the Scherrer equation $\beta \cos(\theta) = k\lambda/D$, where β is the full-width-at-half-maximum of the XRD peaks and k is a constant (k=0.9).
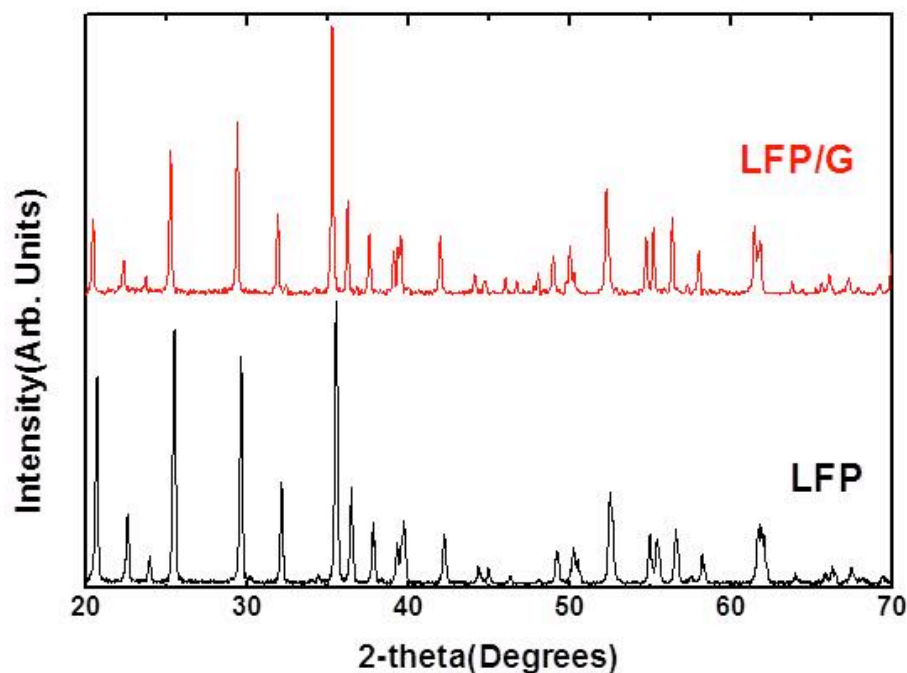
Figure 3.1 XRD patterns of LiFePO$_4$ and LiFePO$_4$/graphene

Figure 3.2(a) shows the Raman spectra of LFP and LFP/G samples along with that of GO powder sample. The LFP sample exhibits all the expected characteristic modes at 950 cm^{-1} (A_g), 998 cm^{-1} (A_g), 1047 cm^{-1} (A_g), and 1069 cm^{-1} (B_{2g}) [72]. However, the LFP modes are barely visible in the Raman spectrum of LFP/G sample because of small penetration depth of low power laser beam through the carbon. The Raman spectra of GO and LFP/G are dominated by two strong G and D modes of graphitic materials which are common features observed in the Raman spectra of disordered carbons [73, 74]. The ratio of the D to G band intensities (I_D/I_G) has been used to study the nature of carbon, in particular, the disorder and the in-plane correlation length [75].

Figure 3.3(b) shows the deconvolution of Raman spectra in the region of D and G bands of GO and LFP/G using Gaussian-Lorentzian peaks.
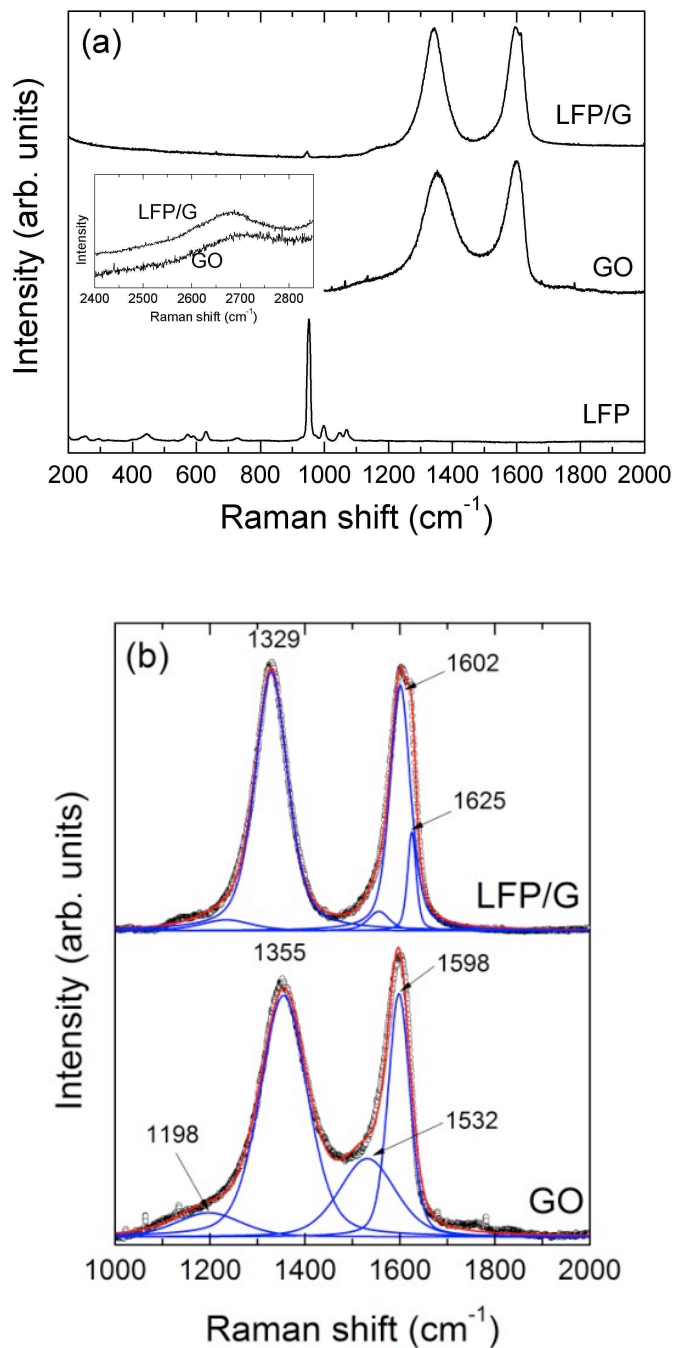
Figure 3.2 (a) Raman spectra of LiFePO$_4$ and LiFePO$_4$/graphene and Raman spectra of GO-pure and LiFePO$_4$/graphene (inset) (b) deconvolution of D and G band

In the case of GO sample, in addition to D and G bands, two more bands (1196 and 1532 cm^{-1}) were necessary to fit the spectrum. These bands have been attributed to poorly organized carbon material outside plane of graphene layers [39]. It is interesting to note that the intensity of these two bands is significantly reduced in LFP/G sample. However, one more band was needed at 1625 cm^{-1} (D' band), in addition to D and G bands, to get a good fitting

The value of I_D/I_G ratio was used to estimate the correlation length (L_a) using [75],

$$L_a = \frac{560}{E_{laser}^4}\left(\frac{I_D}{I_G}\right)^{-1}$$ (3.1)

where, E_{laser} is the Raman excitation laser energy in eV. The calculated value of L_a was 8 nm in GO and 11 nm in LFP/G. This is consistent with the intensity of disorder associated modes at ~1200 and 1530 cm^{-1} being lower in LFP/G compared to GO.

The inset of Fig. 3.3 (a) shows the 2400-2900 cm^{-1} region of the Raman spectra for both GO and LFP/G. It has been shown that the G' or the 2D band ~ 2700 cm^{-1} is sensitive to the stacking order of the graphene sheets along c axis, and has been used to distinguish single and multilayer graphene sheets [75]. Graphene shows a sharp, single 2D Lorentzian peak. But when the number of graphene layers in the stack increases, the band shape changes and tends toward that of a three-dimensional graphite (two Lorentzian peaks). The inset clearly show an enhancement in the intensity of 2D peak ~ 2680 cm^{-1} in LFP/G, compared to that of GO, indicating the reduction of GO to graphene layers in LFP/G.

The reduction of graphene oxide (GO) to graphene in the LFP/G sample is also consistent with the electronic conductivity measurements on both LFP and LFP/G samples. The measured value of electronic conductivity for LFP is 5.0×10^{-8} S cm^{-1} whereas that of LFP/G is 8.4×10^{-2} S cm^{-1}. The six orders of magnitude enhancement in the conductivity indicates that the insulating

GO is successfully reduced to graphene layers during the annealing process, and the graphene sheets in LFP/G likely form a three dimensional conducting network throughout the sample.

Figure 3.3(a) and 3.3(b) shows the Nyquist plots for LFP and LFP/G respectively, with an equivalent circuit in which, R_s represents the resistance between electrolyte solution and electrode, R_{ct} is charge transfer resistance and R_w is called the Warburg resistance. There are two parts of the curve: semicircle and an incline line. Intercept of the semicircle represents R_s and diameter of the semicircle gives the value of R_{ct}. Inclined line represents
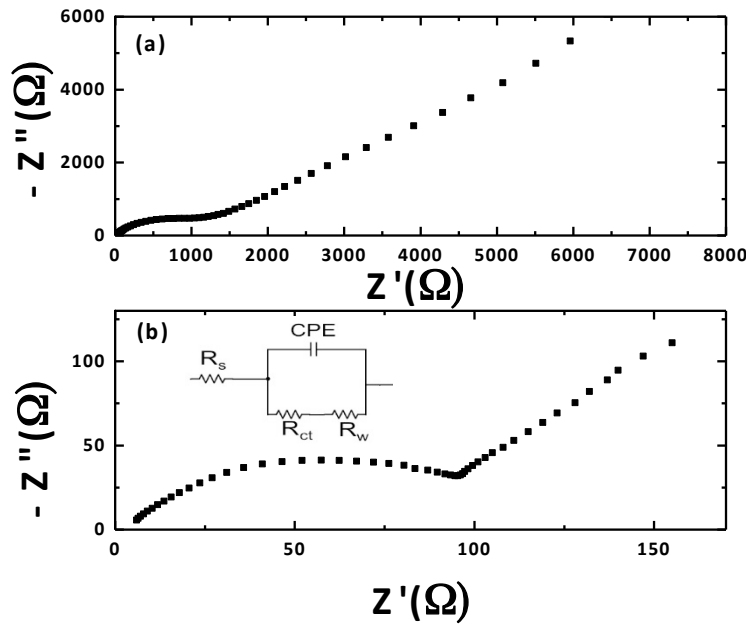
Figure 3.3: Nyquist plots for (a) LiFePO$_4$ (b) LiFPO$_4$/graphene

Warburg's resistance, which is mainly due to ion diffusivity. It is very clear from the two plots that R_{ct} for LFP/G is much smaller than that for LFP. The values for Rct for two samples are 114 Ω and 1.161 kΩ respectively, which infers the higher conductivity in LFP/G than in LFP.

To further confirm that the graphene oxide (GO) in the LFP/G has been reduced to graphene, XPS spectroscopy measurements were performed on GO and LFP/G. As shown in Fig. 3.4, the C1s peak in GO is broader than that of reduced GO in LFP/G.
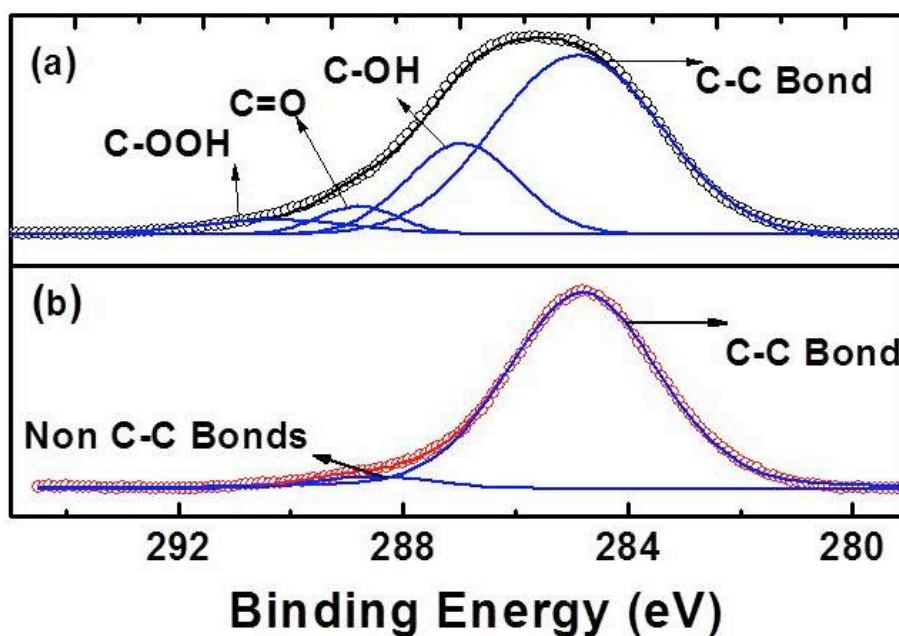
Figure 3.4: Deconvulated C1s XPS peak of (a) graphene oxide GO, and (b) reduced GO in LiFePO$_4$/graphene

This is due to a larger contribution from functional group such as C-OH, C=O, COOH bonds in GO compared to the contribution of these bonds in the C1s peak in LFP/G, which implies the successful removal of C-OH, C=O and COOH groups from the reduced GO in LFP/G. The C1s peak in GO could be de-convolved into four peaks corresponding to the C-C, C-OH, C=O, COOH bonds using asymmetric Gaussian-Lorentzian peak profiles as shown in Fig. 3.5(a). On the other hand, the peak in LFP/G could be de-convolved into two peaks and is strongly dominated by the C-C peak as shown in Fig. 3.4(b). The intensity of the smaller fitted peak is too low to be assigned to any of the known bonds in GO. The binding energies and relative contributions of these four bonds in both GO and LFP/G are tabulated in Table 2.1 [76, 77].

Figure 3.5 shows the SEM and TEM images of both LFP and LFP/G. As shown Fig. 3.5 (a) and (b), both the LFP and LFP/G samples consist of agglomerated nanoparticles. Figure 3.5 (c) shows a low magnification TEM image of the LFP/G sample, where, a good intimate contact

between LFP nanoparticles and graphene sheets can be seen, which explains well the six orders of magnitude higher conductivity in LFP/G than in pure LFP. Dark field image of selected LFP nanoparticle clearly shows that the LFP particles are highly crystalline (Fig. 3.5d), which is further confirmed by the selected area electron diffraction (SAED) as shown in Fig. 3.5(e).

Table 2.1 Binding energy and relative area under the curve of four peaks

Peaks	Energy (eV) and relative area of the peaks for Graphene Oxide (GO)	Energy (eV) and relative area of the peaks for Graphene in LFP/G composite
C-C (sp2)	284.8 (67%)	284.8 (96%)
C-OH	286.3 (23%)	
C=O	288 (5%)	288.5 (4%)
COOH	289.4(5%)	

The room temperature ^{57}Fe Mössbauer spectra for LFP and LFP/G nanocomposite show similar features and consist of two quadrupole doublets (Fig. 3.6 for LFP/G). The first, dominant symmetric doublet with an isomer shift (IS) value ~ 1.23 mm/s and quadrupole splitting, QS ~ 2.96 mm/s is due to Fe^{2+} high spin configuration of the $3d$ electrons and the distorted environment at the Fe atom in LFP [78, 79] . The second doublet with IS ~ 0.47 mm/s and a QS ~0.72 mm/s has been assigned to ferric iron in the sample originating mostly from amorphous impurity phases such as $FePO_4$ and/or Fe_2P produced by high temperature annealing in a partial reducing environment of Ar/H_2 atmosphere [80].
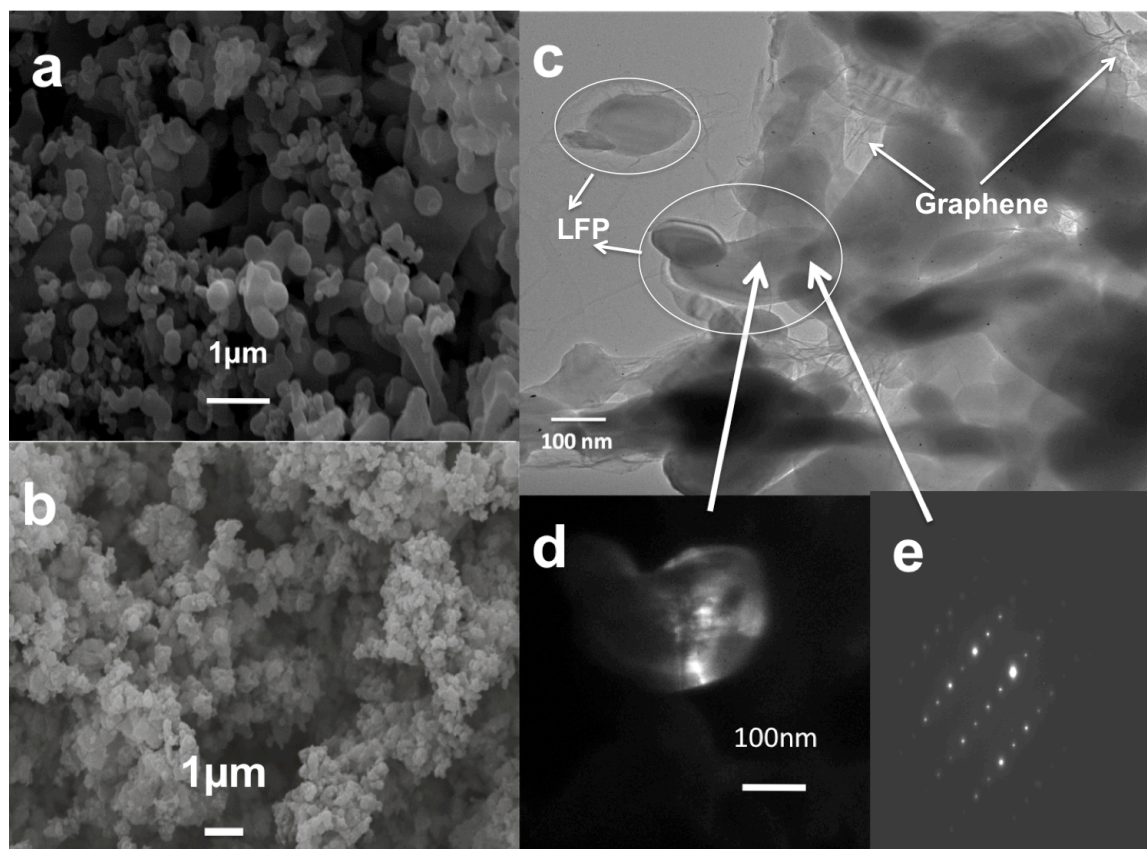
Figure3.5 (a) (b) SEM images of $LiFePO_4$ and $LiFePO_4$/graphene, respectively (c) HRTEM image of $LiFePO_4$/graphene (d) Dark field image (e) SAED pattern of $LiFePO_4$/graphene

The value of IS for this doublet is smaller than that of $LiFePO_4$ likely due to the removal of lithium from $LiFePO_4$, which is accompanied by a decrease of one of Fe $3d$ electron per Fe changing from high spin Fe^{2+} (in $LiFePO_4$) to high spin Fe^{3+} (in $FePO_4$).

As lithium compounds have higher vapor pressure at elevated temperatures, the lithium deficiency in the final compound ($LiFePO_4$) may result even though we used stoichiometric amounts of precursors during the initial synthesis process. This affects the electronic structure near the Fermi surface. The decrease in Fe $3d$ electron also influences the shape of the Fe $3d$ electron density, which is reflected in the decrease in the QS value.
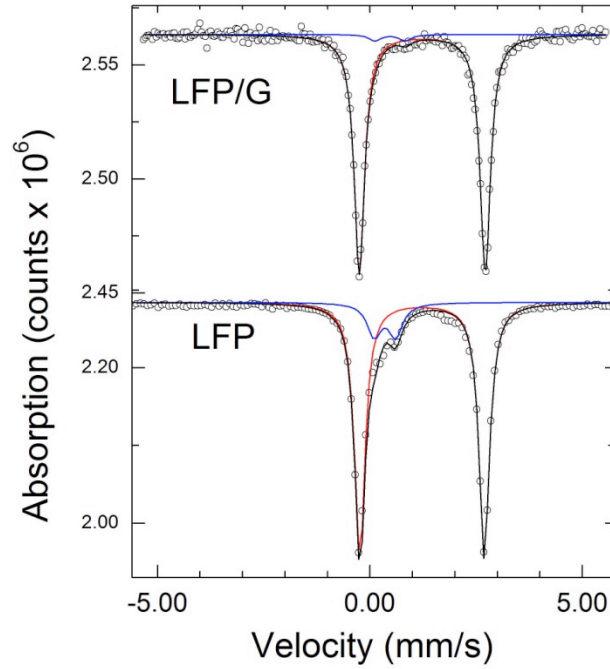
Figure 3.6: Mossbauer spectrum of ^{57}Fe in $LiFePO_4$ and $LiFePO_4$/graphene

The larger line width of the peak for the second doublet indicates the amorphous nature of the phase [80].

We also calculated the amount of the ferrous and ferric iron phases in the samples by estimating the relative area under the respective Mössbauer peaks [81]. For the LFP sample without graphene, the amount of ferrous iron (due to $LiFePO_4$) was 85% and the ferric iron (due to $FePO_4$) was 15%. These amounts changed in the LFP/G sample to 97% due to ferrous and 3% due to the ferric iron. The lower percentage of ferric iron in the LFP/G sample as compared to the $LiFePO_4$ without graphene has been noticed to produce beneficial effects on the capacity,

although the exact role of graphene in lowering the $FePO_4$ impurities is not clear and is the subject of future investigation.

Figure 3.7 (a) shows the charge-discharge voltage profiles as a function of specific capacity for both pure LFP and LFP/G at a charging rate of C/3, where the plateaus indicate the charge-discharge potential of $LiFePO_4/FePO_4$ system. The capacity of LFP/G reaches 160mAh/g, which is close to the theoretical value of 170 mAh/g, while that of LFP is only 65 mAh/g. In addition, the discharge curve of LFP/G is found to be more flat compared to the pure LFP, suggesting that the Li^+ ions can be intercalated/deintercalated more efficiently in LFP/G than in LFP.
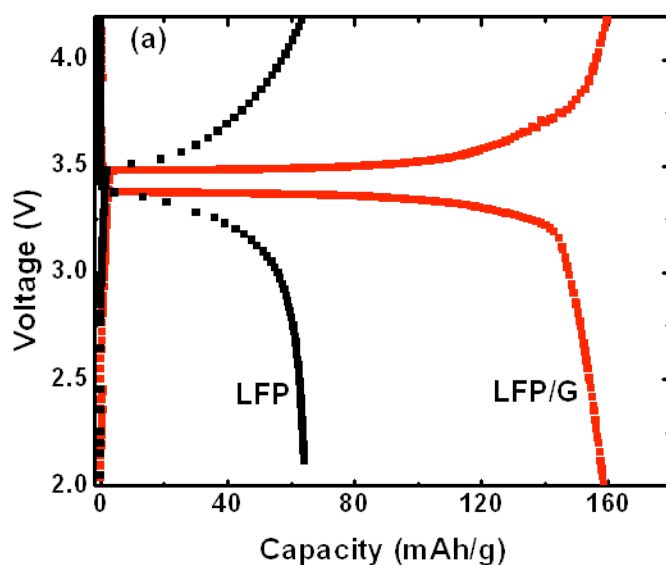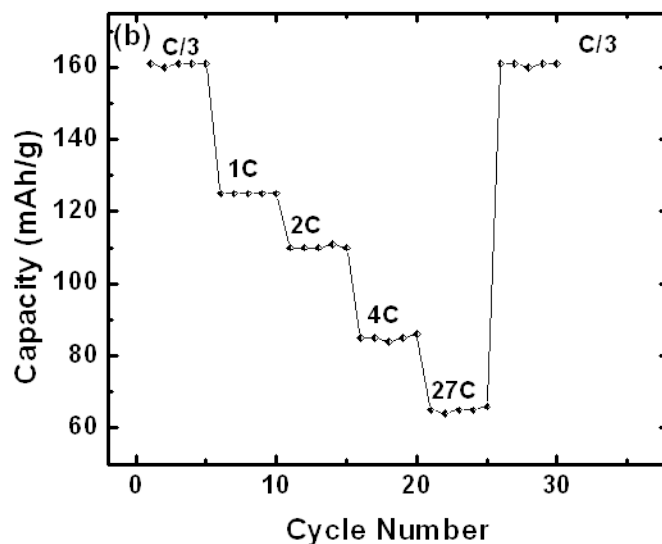
Figure 3.7 (a) Charge-discharge profile for pristine LiFePO$_4$ and graphene wrapped LiFePO$_4$ at C/3 rate. (b) Capacity at different rates for LiFePO$_4$/garaphene

Figure 3.7(b) shows the capacity of LFP/G measured at various charge/discharge rates ranging from C/3 to 27C. Note the capacity of LFP deteriorates rapidly as the rate increases and the cell fails at a rate beyond 1C. On the other hand, the capacity of LFP/G decreases gradually with increasing rate, retaining a reasonable high capacity of over 90 mAh/g at 4C. The cells with LFP/G cathode work even at a very high rate of 27C, though the capacity reduces to 60 mAh/g. After going through the cycles of various charging/discharging rates, the cells with LFP/G were tested again at C/3 and no reduction in capacity was observed. To further investigate the stability of the capacity versus cycle life, the cells were subjected to large number of cycles at 1C rate. As shown in Fig. 3.7(c), a capacity value of ~126mAh/g is observed even after 500 cycles, indicating very high cyclic stability of the LFP/G as a cathode material for Li-ion batteries. It is worth noting that these remarkable properties were achieved by adding only 5% active carbon during the cell preparation, while about 10-20% of active carbon is traditionally added. In case of

conventional carbon coating on LFP particles, most researchers have reported up to a maximum of 100 cycles [82-84]. All these improvements in the electrochemical performance of LFP/G may be ascribed to the huge improvement in electronic conductivity (around six orders of magnitude), which is the result of better contact between LFP nanoparticles and graphene sheets. In addition, the highly flexible graphene sheets in the LFP/G composite may also reduce the agglomeration of the LFP nanoparticles, hence allowing easier exchange of Li^+ ions and electrons between the LFP and the electrolyte.
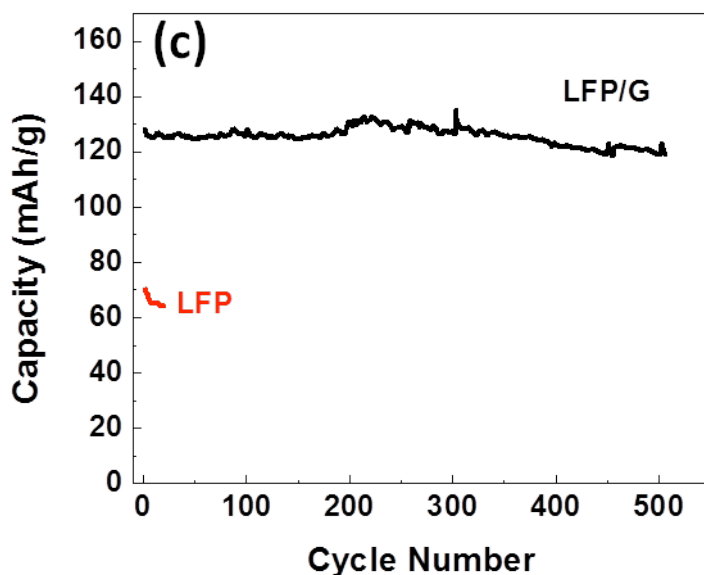
Figure 3.7 (c) Capacity Vs cycle number at 1C for $LiFePO_4$ and $LiFePO_4$/graphene

3.5 Conclusion

In conclusion, we have successfully prepared LFP/G composite using a simple sol-gel method. The addition of graphene to LFP significantly improves the capacity and capacity retention of LFP as a cathode material for Li-ion batteries. Annealing at $600^{o}C$ for 5 hrs in Ar/H$_2$ sufficiently reduces the graphene oxide to graphene as confirmed by Raman spectroscopy, electrical conductivity and XPS measurements. Mössbauer spectrum confirms that our LFP/G is

highly pure with very small amount (~3%) of an impurity phase. TEM images of LFP/G show that graphene sheets form a three-dimensional conducting network throughout the sample and provide an easy path for the electrons and Li-ions during the charging/discharging processes. At low C rate, the capacity of LFP/G approaches the theoretical value. More importantly, the LFP/G demonstrates a much better rate capability and drastically improved cyclic stability than LFP. This work suggests that the electrochemical performance of LEP can be substantially improved by adding graphene during the synthesis, even if we do not control the particle size.

CHAPTER 4

TEPERATURE DEPENDENT STUDY OF IMPURITIES IN LiFePO$_4$/C NANOCOMPOSITES AND THEIR IMPACT ON ELECTROCHEMICAL PERFORMANCE

4.1 Introduction

Incorporation of conducting metal phases into LiFePO$_4$ is reported to be a viable method to enhance the electronic conductivity of the material [47, 85, 86]. Iron phosphide Fe$_2$P is known to be a very good electronic conductor [21]. Olivine phosphates, particularly LiFePO$_4$, are known to undergo carbothermal reduction at high temperatures to form Fe$_2$P and other metal phosphides. In the presence of enough carbon at high temperatures, carbon reacts with LiFePO$_4$ to form CO$_2$ or CO, which results into two-phase system Li3PO4/Fe$_2$P [87]. So the conducting phase Fe$_2$p can be generated intrinsically in LiFePO$_4$. Incorporation of Fe$_2$P in LiFePO$_4$ has shown an improvement in electrochemical performance as it provides conducting network to facilitate the electron mobility through the material. It has been shown that even a small quantity of Fe$_2$P can enhance the electronic conductivity by 4 orders of magnitude [88]. However, excessive amount of this conducting phase may result in loss of capacity as it forms at the cost of LiFePO$_4$, which is responsible for lithium intercalation/deintercalation [89]. There are several studies, which reported the effect of addition of Fe$_2$P on the electronic as well as electrochemical properties of LiFePO$_4$ [90-92].

Y. Liu *et al*., prepared LiFePO$_4$ with co-precipitation method and found that the use of in-situ polyacricamide (PAM) (Carbon source) provides reducing environment to form Fe$_2$P [93].

They heated the as prepared $LiFePO_4$ to various temperatures and found that Fe_2P appears only at 750^oC. Authors reported that sample which showed traces of Fe_2P exhibits better electronic conductivity and capacity over the others. Although, quantification of Fe_2P was not reported, they found an increase in Fe_2P with calcination time along with an improvement in capacity. Rahaman *et al*., synthesized $LiFePO_4$-Fe_2P-C material using solvent assisted solid state reaction with various amounts of citric acid as a source of carbon [94]. They found that the use of solvent assists the formation of Fe_2P in the proximity of $LiFePO_4$ particles, which provides a percolating network resulting in very high electronic conductivity. Authors claimed a very high capacity 136 mAh/g at 10C with 96% retention in capacity after 1000 cycles (references). Prepared by mechanical alloying and subsequently heated at 900 $^{\circ}C$ for 30 min. Kim et al found that sample containing 8% Fe_2P showed the best capacity of 160 mAh/g at C/20 [95]. Lin et al, however reported presence of FeP is more favorable over Fe_2P [96]. At a rate of 1C the capacity of the sample with Fe_2P was 90 mAh/g and that with FeP is 110 mAh/g. They argued that the amount of Fe_2P (16%) is more than required. So from the above literature review, we infer that Fe_2P phase appears at high temperatures and is favorable to the electrochemical performance of $LiFePO_4$. Although, Rahaman and coworkers reported very good rate capability, correlation between amounts of Fe_2P and the capacity, optimum amount of Fe_2P still needs to be examined carefully. So a detailed study correlating the electrochemical performance with the quantification of Fe_2P is valuable. In this paper, we report an extensive temperature dependent study on $LiFePO_4$/C prepared by a simple and cost effective sol-gel method followed by calcination in reducing Ar/H_2. We have synthesized samples at various temperatures and quantified the Fe_2P using magnetic and Mössbauer spectroscopy measurements. We have found that annealing at $700^{\circ}C$ yields optimum amount of Fe_2P without increase in particle size and hence shows the best

capacity and high rate capability. We further demonstrate that excessive amount of Fe_2P deteriorates the capacity.

4.2 Experimental Details

4.2.1 Synthesis of LiFePO$_4$/C

We used sol-gel method to synthesize LiFePO4/C. Starting synthesis technique has been reported in our earlier work [97]. In a typical synthesis process $CH_3COOLi \cdot 2H_2O$, 99% (Alfa Aesar), $FeCl_3$ (Fisher Scientific) and P_2O_5 (Fisher Scientific) were used as precursors. FeCl3 and P2O5 were dissolved in 200 proof ethanol in two separate beakers and then mixed and stirred for 3 hours in a three-neck flask under constant flow of nitrogen. Then lithium acetate dissolved in ethanol was added to the solution and was allowed to stir for additional 3 hours. Lauric acid dissolved in ethanol was added as a source of carbon and solution was kept 3 more hours of stirring under the same conditions. After that the solution was dried at 90ºC to form a dry gel, which was subsequently calcined at 600, 700, 800, 900ºC for 10 hours and one batch at $900^{\circ}C$ for 20 hours under the flow of Ar/H_2 (90%/10%). Hereafter, samples will be referred to as LFP-600, LFP-700, LFP-800, LFP-900 and LFP-900-20, respectively.

4.2.2 Characterization

X-ray diffraction (XRD) measurements were performed on the sol-gel synthesized samples to determine their phase purity using a Rigaku Minflex-600 diffractometer equipped with a Cu K-α (λ=1.54 Å) x- ray source. Magnetic measurements were carried out with Physical Properties Measurement System (PPMS). Temperature dependent ac magnetization measurements were

done at 500 Oe and saturation magnetization (M) was measured by varying the magnetic field (H) from -5T to +5T.

The morphology of the samples was investigated using JOEL JSM-6510-LV-LGS SEM. [57]Fe Mössbauer spectra were recorded in the transmission geometry using both sides of a (Wissel) transducer coupled to [57]Co in Rh matrix source of about 50 mCi and 256 channels of a multichannel analyzer. The velocity calibration and the linearity verification were performed using a thin iron foil. For Mössbauer measurements, approximately 70 mg of the sample was uniformly distributed in a Teflon circular cell of 1.7 cm diameter. The isomer shift values are reported with reference to α-Fe foil. The spectra were least square fitted with MossWin program. Electrochemical Impedance spectroscopy measurements were carried out using Gamry electrochemical system in the frequency region of 0.01 Hz-100 kHz with AC amplitude 10 mV.

4.2.3 Fabrication of electrochemical cell and electrochemical measurements

The electrochemical characterization of the samples was performed using standard coin cell geometry with lithium metal as an active anode. The active cathode materials and Super P as a conducting material were mixed (95:5 ratio) and ground for 20 min (without binder). The homogenous mixture was then put on an aluminum mesh and mesh and mixture was hand pressed between two steel cylinders. This mesh acts as a current collector. The method of cathode preparation has been reported earlier [97]. The prepared cathode was cycled against Li metal electrode as a counter electrode separated by a polymeric separator soaked in a binary electrolyte consisting of ethylene carbonate (EC) and dimethyl carbonate (DMC), (50:50) containing 1M $LiPF_6$. The room temperature galvanostatic charge and discharge measurements were carried out at different C-rates in the voltage range 2.2 – 4.2 V.

4.3. Results and Discussion

Figure 4.1 shows XRD pattern of all LiFePO₄ sapmles annealed at 600-900℃ for 10 hours and a LiFePO₄ sample annealed at 900℃ for 20 hours.
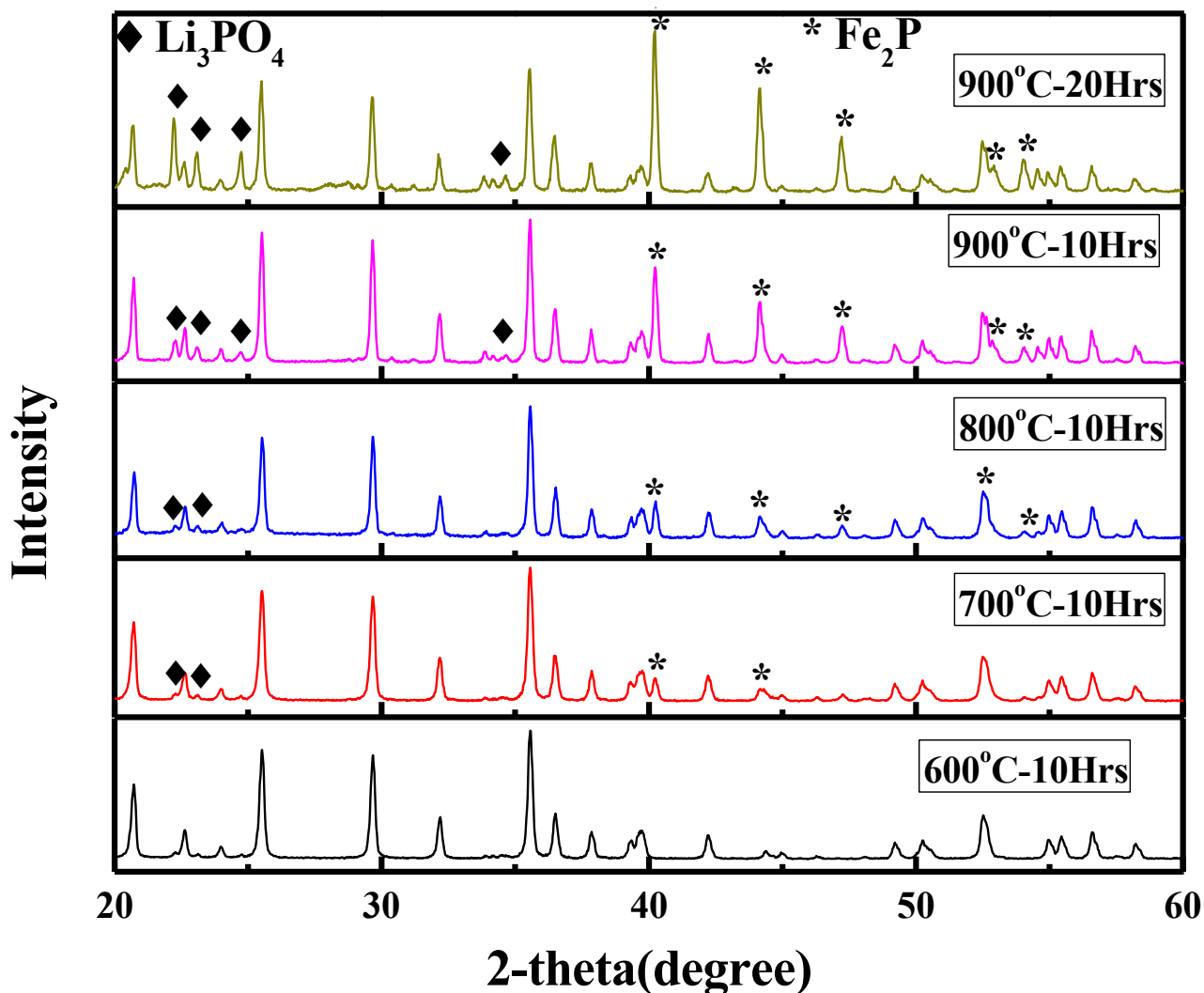
Figure 4.1. XRD pattern of LiFePO₄/LA annealed for 10Hrs at (a) 600℃ (b) 700℃ (c) 800℃ (d) 900℃ and for 20 Hrs at (e) 900℃

In the LFP sample annealed at 600 °C, all the Brag peaks observed can be indexed to olivine structred LiFPO₄ with space group Pnma, which implies there is no detectable impurity phase. These peaks can also be found in all the higher temperatue annealed samples confirming that olivine structure was preserved at higher temeratures as well. Aditional peaks were observed

startng at 700 ^{o}C which were indexed to iron phosphide (Fe$_2$P) and Li$_3$PO$_4$. The latter phases appears to grow significantly only at 900 $^\circ$C. These peaks result from carbothermal reduction of LiFePO$_4$ at higher temperatures in reducing environment provided by the lauric acid (carbon source) and the flowing forming gas. It can be seen that annealing at higher temeratures results in an increase in impurity phase. As the formation of Li$_3$PO$_4$ requires three Li ions, this phase does not grow as quickly as Fe$_2$P because dissociation of LiFePO$_4$ is not fast enough upto 700 $^\circ$C. They starts to show up considerably only at 800 $^\circ$C and higher temperatures.

Since Fe$_2$P is magnetic with first order ferromagnetic transition at ~220 ^{o}C [98, 99], magnetic property measurements were done to further confirm the existence of Fe$_2$P. Zero field cooled (ZFC) temperature dependence of magnetization at an applied field of 500 Oe was measured and is displayed in Figure 4.2. Although not observable in the XRD, first order ferromagnetic transition at ~220 $^\circ$C due to Fe$_2$P can be observed in all the samples but it is rather weak in LFP-600, whereas it is quite clear in samples annealed at higher temperatures due to an elevated amount. .
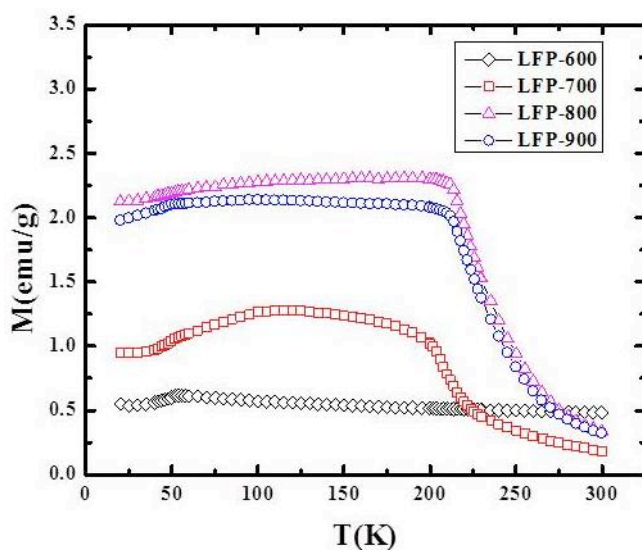
Figure 4.2 Magnetization vs. Temperature of LiFePO$_4$ samples
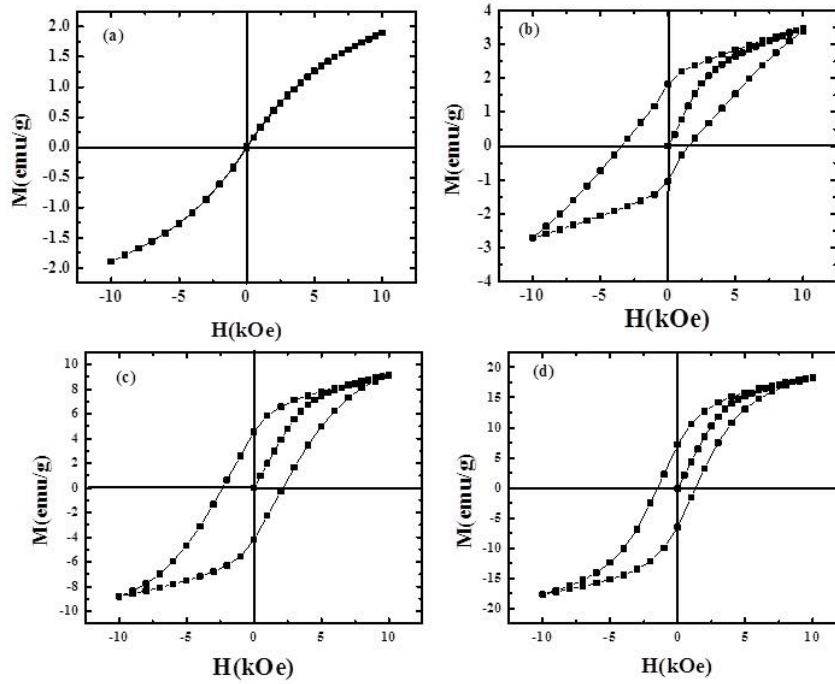
Figure 4.3. Hysteresis loops measured at 10K for LiFePO$_4$/LA annealed for 10Hrs at (a) 600℃ (b) 700℃ (c) 800℃ (d) 900℃

of ferromagnetic Fe$_2$P phase. Thus XRD and magnetization measurements confirm the presence of Fe$_2$P in all the samples and also demonstrate an increase in the amount as temperature increases.

As discussed earlier in the introduction part, the amount of Fe$_2$P has a significant impact on the specific capacity. Figure 4.3 shows the measured hysteresis loops of magnetization vs applied field for all the samples. It can be clearly observed that the magnetization increases with increasing annealing temperature. Although magnetization was not saturated in the applied field of ±10kOe, maximum magnetization achieved in each sample was compared with magnetization value of pure Fe$_2$P reported earlier in literature [100]. The saturation magnetization reported for Fe$_2$P is 35 emu/g. Considering this value as 100%, estimated amount of Fe$_2$P in LFP-600 to LFP-

900 is 5%, 15%, 32% and 50%, respectively. As a result, the amount of active material for Li intercalation/deintercalation is substantially reduced in LFP-800 and LFP-900, which is expected to lower the overall specific capacity.

To further confirm the amount of Fe_2P as determined by magnetization measurement, Mössbauer spectra were collected and are shown in Figure 4.4. [57]Fe Mössbauer spectra consists of three quadrupole doublets. First, symmetric and dominant doublet with isomer shift ~1.22 mm/s and quadrupole splitting of ~2.97 mm/s is due to high spin configuration of $3d$ electrons in Fe^{2+} ion and environment distortion around Fe in parent $LiFePO_4$ [101, 102]. The two different favorable sites for Fe^{3+}, namely tetrahedral 3(f) and pyramidal 3(g) in structure of Fe_2P, cause two distinct doublets in the Mossbauer spectrum [100]. The second doublet with isomer shift of 0.61 mm/s is due to Fe^{3+} occupying site 3(f) in Fe_2P while third at 0.97 mm/s is due to Fe^{3+} at pyramidal 3(g) site. A very small signature of one of the two doublets for Fe_2P in LFP-600 indicates a very small amount of Fe_2P occupying Fe- site only. Higher values of isomer shift and quadrupole splitting for first doublet is due to the presence of one extra electron in outer $3d$ orbital of Fe^{2+}, which makes it high spin and causes distorted environment around the nucleus. Mössbauer parameters for other two doublets are relatively smaller as half filled $3d$ orbital provides a more stable environment. We have estimated the amount of Fe^{2+} and Fe^{3+} from the relative area under the respective curve in Mössbauer spectra. The percentage of Fe^{2+} and Fe^{3+} phase is listed in Table 4.1. It is interesting that the total amount of Fe_2P calculated from Mössbauer measurements is very close to what is estimated from the magnetic measurements.
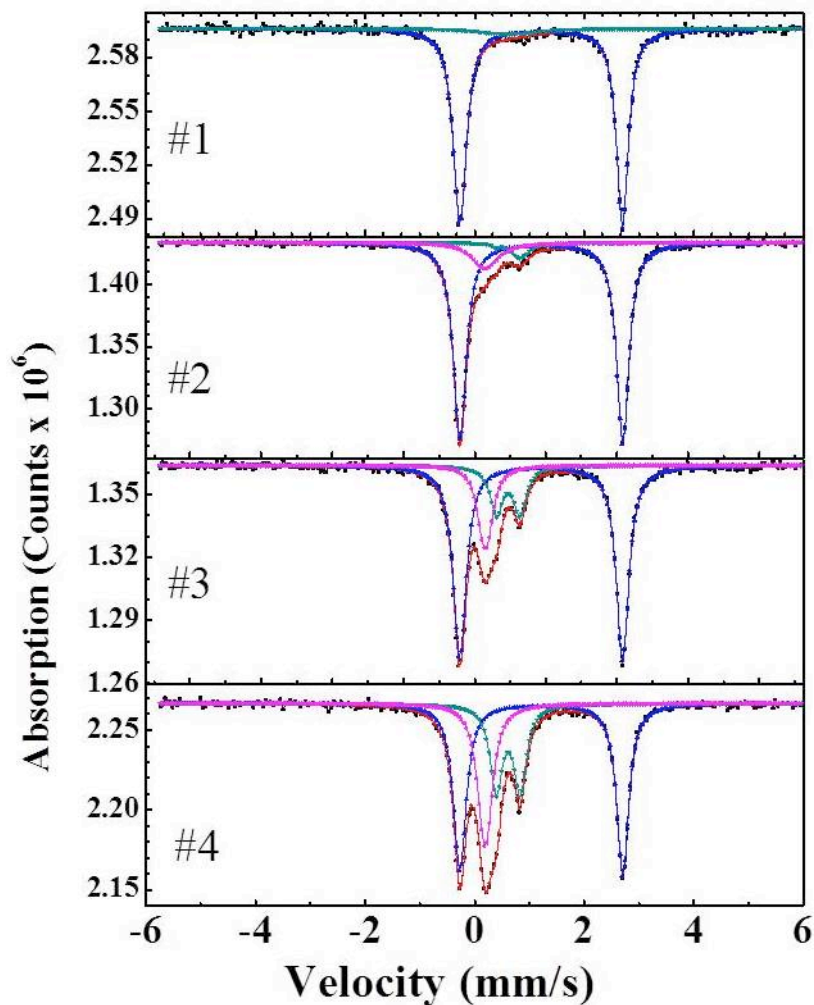
Figure 4.4. Mossbauer Spectra of LiFePO$_4$ (1) LFP-600 (2) LFP-700 (3) LFP-800 and (4) LFP-900

Figure 4.5 shows SEM images of all the 10 hour annealed samples. The particle size of samples annealed at 600 °C and 700 °C appears to be similar and uniform except in some agglomerated regions as shown in Figure 4.5(a) and (b). The average particle size for these two sample is estimated to be ~ 100 nm.

Table 4.1. Mossbauer parameters of all the samples

	LFP/LA-600C	LFP/LA-700C	LFP/LA-800C	LFP/LA-900C	
DOUBLET (1)	94.7 %	83.9%	67.6%	50.3%	Fe^{2+}
DOUBLET (2)	5.3%	4.8%	16.3%	25.2%	Fe(1) site of Fe_2P
DOUBLET(3)	-	11.3%	16.1%	24.5%	Fe(2) site of Fe_2P
Fe_2P	5.3%	16.1%	32.4%	49.7%	
Capacity (mA h/g) at 1C	130	160	110	100	

However, a noticeable grain growth and increased nonuniformity can be observed in the LFP-800 sample, which continues to be observed in the sample annealed at $900^{\circ}C$ (Figure 4.5 (c) and (d)). Some particles are as large as 500-600nm in the LFP sample annealed at $800^{\circ}C$ and even exceede 1μm in the LFP-$900^{\circ}C$ sample. The relatively small size of the particles and uniform distribution in samples annealed $600^{\circ}C$ and $700^{\circ}C$ can be attributed to a particle growth inhibiton due to the uniform coating of Fe_2P around the $LiFePO_4$.
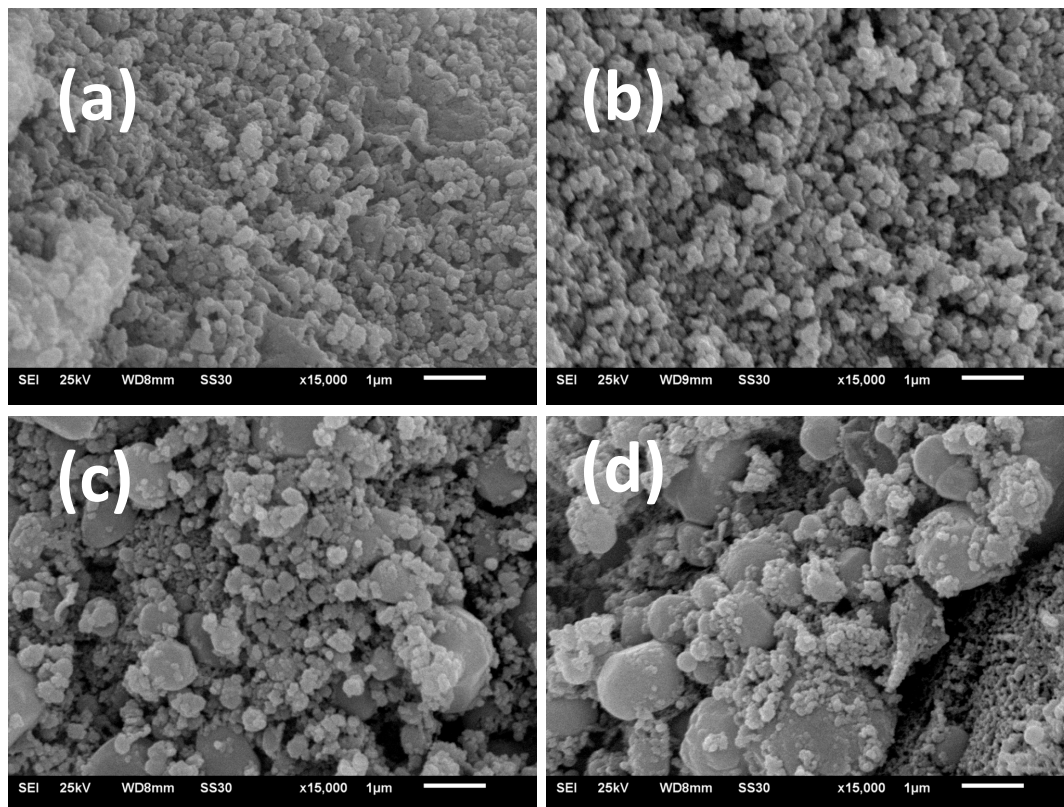
Figure 4.5 SEM images of LiFePO$_4$/LA annealed for 10Hrs at (a) 600℃ (b) 700℃ (c) 800℃ (d) 900℃.

Figure 4.6 (a) shows charge-discharge voltage profile with respect to specific capacity of all the samples at a discharging rate of 1C where the plateau illustrate the redox potential of two phase LiFePO$_4$-FePO$_4$ system. LFP-700 delivers a capacity of 160 mAh/g at 1C, which is reasonably close to the theoretical capacity of 170 mAh/g whereas LFP-600, LFP-800 and LFP-900 show relatively lower capacities of 129 mAh/g, 110 mAh/g and 86 mAh/g respectively. In addition dischargecurve for LFP-700 shows a wider flat region, which indicates that Li can be intercalated and deintercalated more efficiently. Trend of specific capacity values obtained for various samples from voltage profile in Figure 4.6(a) is in accordance with the information revealed from Nyquist plots shown in Figure 4.6(b), which consist of two distinctive parts: diameter of the semicircle reresents charge transfer resistance (R$_{ct}$) whereas inclined line is Warburg behaviour.
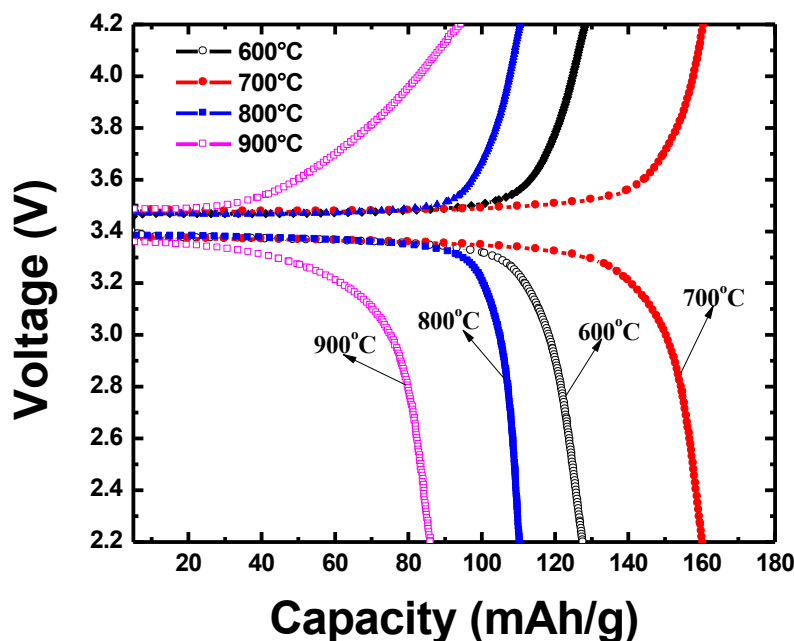
Figure 4.6 (a) Charge-discharge profiles of LiFePO$_4$/LA annealed for 10Hrs at 600 ºC, 700 ºC, 800 ºC and 900 ºC at

a rate of 1C

Values for charge transfer resistance extracted from the plots shown in 4.6(b) for LFP-600 to

LFP-900 are 170Ω, 52Ω, 90Ω and 115Ω respectively. LFP-700 exhibits the lowest charge

transfer resistance and hence highest specific capacity suggesting that amount of Fe$_2$P is

optimum to provide highly conducting network, which facilitated the electron mobility. Lowest

charge transfer resistance for LFP-700 is due to improved electronic conductivity. An anomoly

in correlation of specific capacity to charge transfer resistance can be observed when we

copmare the two values for LFP-600 sample and 800 ^{o}C,900 ^{o}C samples. Although higher

temerature annealed samples have lower charge transfer resistance due to existance of large

amount of Fe$_2$P, less active material for Li intercalation and deintercalation causes the capacity

to drop to lower values.
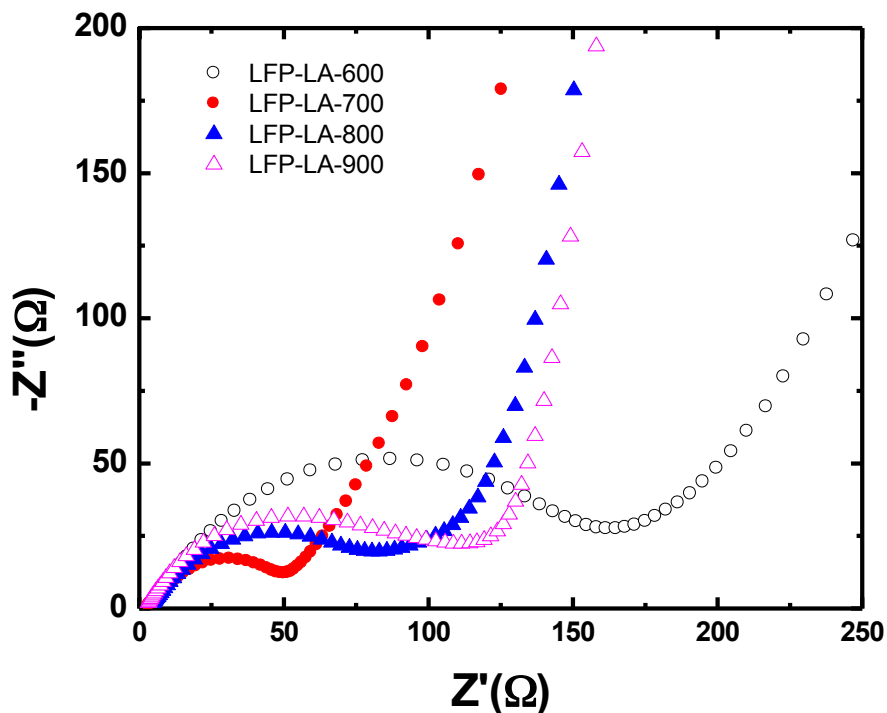
Figure 4.6(b) EIS spectra of LiFePO$_4$/LA annealed for 10Hrs at (a) 600 ^{o}C (b) 700 ^{o}C (c) 800 ^{o}C (d) 900 ^{o}C

It is intersting to note that LFP-800 delivers almost 100% specific capacity (110 mAh/g) of the available active material, which is around 68% of the composite, indicating that the entire particles can be intercalated due to high electronic conductivity provided by Fe$_2$P in spite of the relatively large particle size.

Figure 4.6(c) shows the discharge capacity of all the samples at various rates from 1C to 10C. LFP-700 not only shows the best capacity at lower rate but also retains the very good capacity at higher rates. It is remarkable that after showing 160 mAh/g at 1C, it delivers 142 mAh/g when tested at a rate of 10C, retaining about 89% of capacity with 10 times increase in rate. To best of our knowledge, this is the highest reported capacity at this rate so far. The other samples show much lower capacity at this high rate (600 ^{o}C-98 mAh/g, 800 ^{o}C-82 mAh/g and 900 ^{o}C- 68 mAh/g). This finding indicates that Fe$_2$P enhances the electronic conductivity and

hence the specific capacity, but at the same time excessive amount of Fe_2P leads to the deficiency of active material leading to a lower capacity. All the improvements in electrochemical properties of $LiFePO_4$ at 700 ℃ can be ascribed to high electronic conductivity which is due to existance of homogeneously mixed Fe_2P conducting phase in an appropriate amount.
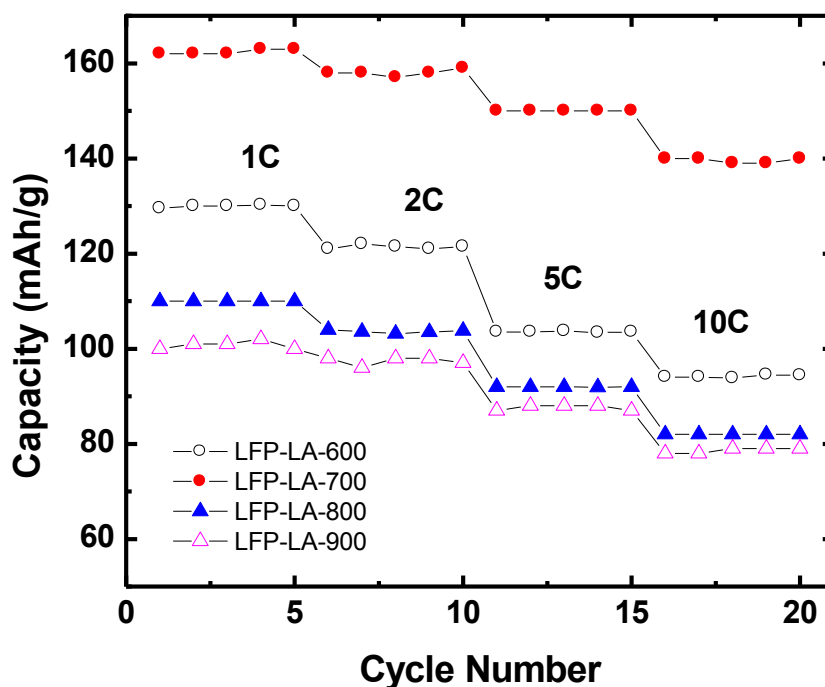
Figure 4.6(c) Capacity at various rates (1C to 10C) of LFP samples

Additionally, LFP-700 shows 158 mAh/g and 155 mAh/g at rate of 2C and 5C, which can be considered as close to the theoretical capacity.

4.4 Conclusion

In conclusion,we have successfully prepared $LiFePO_4/C$ by sol-gel method followed by calcination at various temperatures. Growth of Fe_2P phase at higher temperatures was detected by XRD and magnetic measurements and was further quantified by Mossbauer spectrocopy.

Existance of Fe_2P significantly enhances electronic conductivity and hence charge tranfer resistance. Particle size as well as the amount of electrochemically inactive Fe_2P grows considerably at 800 °C and 900 °C but all the availble lithium can be intercalated because of high electron mobility . LFP-700 contains about 15% of Fe_2P, which is sufficient to bring huge improvement in charge transfer resistance without much compromise in the quantity of active material. It shows a capacity of 160 mAh/g at 1C and 142 mAh/g at 10C with a charge transfer resistance of 52 Ω. This work suggests that controlling the reduction environment and temperture during the synthesis process can tune the amount of conducting Fe_2P to optimum for best capacities at higher rates.

CHAPTER 5

EFFECT OF INDIUM DOPING ON ELECTROCHEMICAL PROPERTIES OF LiFePO$_4$

5.1 Introduction

As discussed in the previous chapters, carbon coating helps to improve the electrochemical properties of LiFePO$_4$. In addition to the traditional carbon coating, doping has also attracted interest. In LiFePO$_4$, there are two sites of interest from doping point of view: lithium site and iron site. Various ionic elements such as isovalent ions (Mn, Co, Ni, Zn), supervalent ions (Al, Ti, Zr, Nb) heterovalent ions (Nd, Gd) have been successfully used to dope LiFePO$_4$ without lattice distortions [13, 103, 104]. Wang et al studied the effect of doping Mg on lithium M-1 site and found 4 orders of magnitude improvement in electronic conductivity [105]. They prepared both stoichiometric and non-stoichiometric samples of Li$_x$Mg$_y$FePO$_4$ with x= 0.97, 0.98, 0.99 and y=0.005, 0.01, 0.02 and found that stoichiometric Li$_{0.99}$Mg$_{0.01}$FePO$_4$ to show the highest electronic conductivity. Liu and coworkers prepared LiFe$_{0.9}$Mg$_{0.1}$PO4 by doping Mg at Fe site and observed a slight shrinkage of the unit cell without affecting the overall olivine structure [106]. They reported that Mg doped sample exhibits 130 mAh/g at rate of 2C whereas undoped LiFePO$_4$ showed 115 mAh/g at same rate. Roberts *et al* compared the doping of Mg on both Li and Fe sites by preparing Li$_{1-x}$Mg$_{x/2}$FePO$_4$ and LiFe$_{1-y}$Mg$_y$PO$_4$ with varying amounts of carbon source. They noticed that with increase in x and y, a higher amount of carbon was required to maintain the capacity value and also found that LiFe$_{0.99}$Mg$_{0.1}$PO$_4$ gives best results. Ni *et al* [107] reported enhancement in electronic conductivity by doping with Mg, Cu and Zn

and showed that ion doping improves electrochemical properties. Liu *et al* [108] reported that doping with Zn via solid-state method assists the crystal growth and also expand the lattice, providing more space for Li ion intercalation/deintercalation. They have also shown an improvement in charge transfer resistance by doping with Zn. Shenauda *et al* [109] followed this study by using ZnO as a precursor in different amounts for doping. They prepared undoped LiFePO4 with 1.5%, 2.5% and 5.0% ZnO and found that 2.5 % is the optimum amount to achieve the best capacity of 177 mAh/g. The lower charge transfer resistance and more flat plateau around 3.48V indicate that the two phase nature of the reaction is responsible for the high capacity. However, they have not reported high rate capacities. Shi and coauthors [110] reported eight orders of magnitude increase in electronic conductivity by doping the higher valence Cr^{+3}, calculated from first principle calculations that was confirmed by experiments. Yang and coworkers doped Cu^{2+} ion in LiFePO4 to obtain $Li_{0.98}Cu_{0.1}FePO_4$ [111]. Larger radius of copper ion compared to the lithium ion and also stronger force between copper ion and oxygen in the compound causes shrinkage of the unit cell. Copper doped $Li_{0.98}Cu_{0.1}FePO_4$ showed better capacity (155 mAh/g) compared to undoped $LiFePO_4$ (130 mAh/g). Heo *et al* [112] prepared Cu doped samples with stoichiometric and non-stoichiometric lithium amount. They found that Cu doped sample with excess amount of lithium delivered the best capacity and cycling stability.

In this study, we chose In for doping at the Fe site. Substitution of Li at Fe site seems favorable as both ions have similar value of electronegativity and ionic radius. So we present the synthesis and characterization of 1 mol% In doped LiFePO4 in this chapter.

5.2 Experimental Details

In-LiFePO4 (LFP-In) was prepared by sol-gel method using lithium acetate dihydrate, 99% (Alfa Aesar), ferrous chloride (Fisher Scientific), phosphorous pentoxide (Fisher Scientific)

and indium chloride as precursors. Ferrous chloride and phosphorus pentoxide were dissolved in 200 proof ethanol and mixed in a flask. 1 mol% of indium chloride dissolved in ethanol was added to the solution and stirred for 3 hours in nitrogen atmosphere. Then the lithium acetate, also dissolved in 200 proof ethanol, was added to the solution and allowed to mix for another 3 hours under nitrogen atmosphere. Subsequently, 0.75M lauric acid was added to the solution. This mixture was allowed to mix for an additional 3 hours and then the sample was dried at 85 ^{o}C. The resulting gel was annealed at 600°C (LFP-In-600), 700°C (LFP-In-700) and 800°C (LFP-In-800) for 10 hours with a constant flow of forming gas (90% Ar and 10% H_2).

5.3 Results and Discussion

Figure 5.1 shows the x-ray diffraction pattern of LFP-In-600, LFP-In-700 and LFP-In-800.
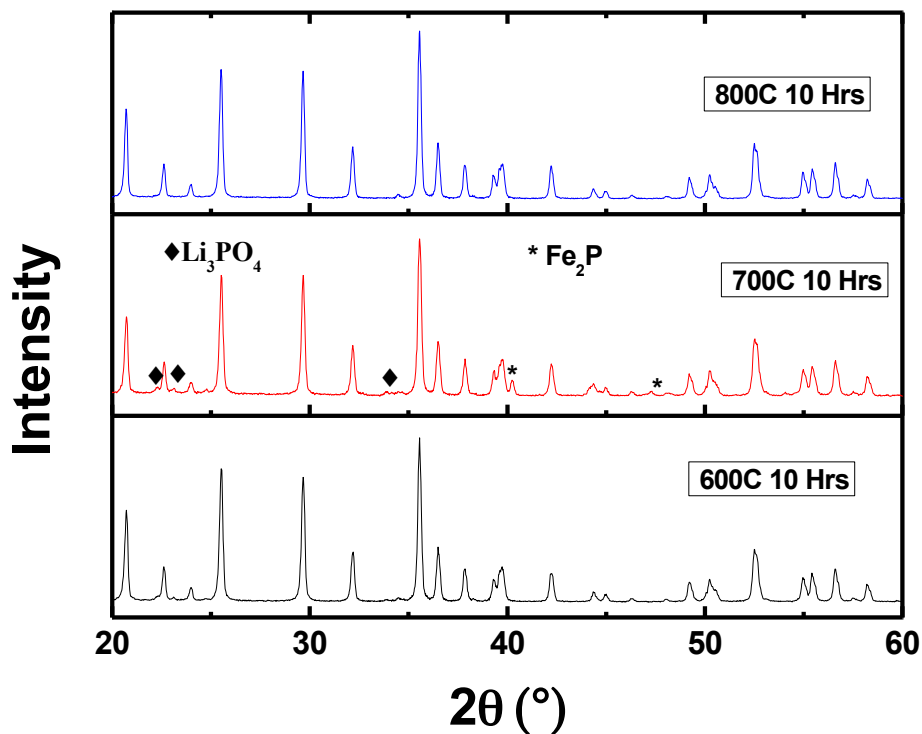
Figure 5.1. XRD pattern for LFP-In-600 , LFP-In-700 and LFP-In-800

Clearly, all the main sharp and intense peaks can be indexed to Bragg's peaks for the olivine structure of $LiFePO_4$ in all the samples indicating that addition of indium as dopant does not affect the original structure of $LiFePO_4$. But when temperature is 700 °C, Fe_2P peaks appear in the pattern with main peak around 41°, which is surprisingly absent in the sample annealed at 800 °C.
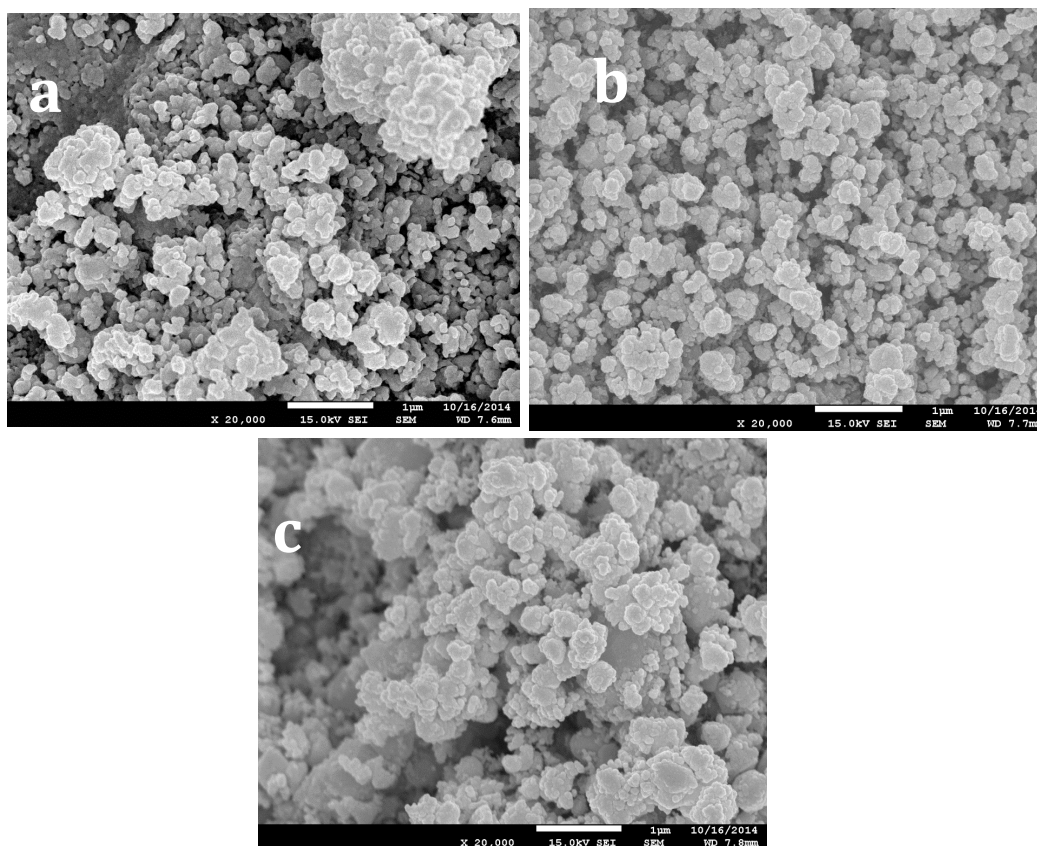
Figure 5.2. SEM images of (a) LFP-In-600 (b) LFP-In-700 (c) LFP-In-800

SEM images for all the samples are shown in Figure 5.2. Although particle size appears to be the same, less agglomeration and more uniformity can be observed in LFP-In-700 as compared to LFP-In-600. On the other hand, the particle size in LFP-In-800 becomes less uniform as some bigger particles can be seen underneath smaller particles. Less agglomeration in

LFP-In-700 can be ascribed to carbon coating achieved at lower temperature, which reduces the chances of agglomeration.

Mössbauer spectroscopy was performed on LFP-In-600 and LFP-In-700 to further quantify the small amount of Fe_2P found in the XRD pattern as shown in Figure 5.3.
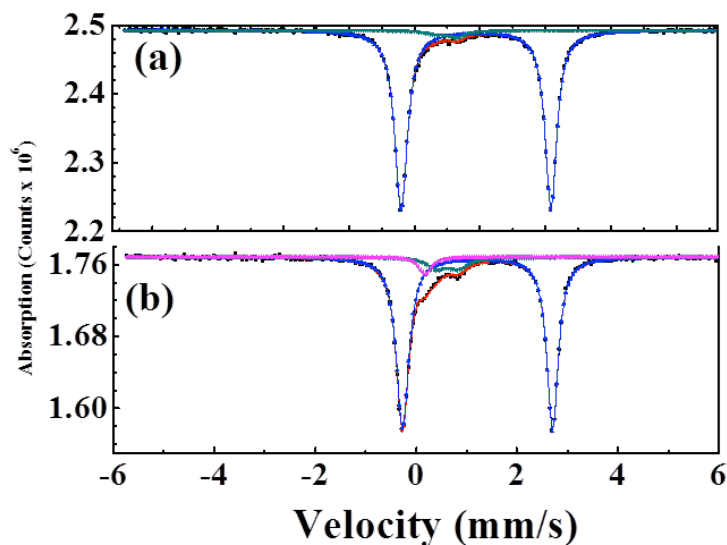
Figure 5.3 Mössbauer spectra of (a) LFP-In-600 and (b) LFP-In-700

Mössbauer parameters are shown in Table 3. First doublet is due Fe^{2+} in $LiFePO_4$ and has larger isomer shift and quardupole splitting due to its high spin. In LFP-In-600 there is small amount of Fe_2P, where Fe occupies site 1, which could not be detected in XRD. LFP-In-700 contains more Fe_2P and amount of Fe is distributed on both available sites totaling 13.3%. Charging/discharging curves in Figure 5.4 show a typical $LiFePO_4$ behavior with a plateau at about 3.5V. This plateau is longest in case of LFP-In-700, which contributes to most of the capacity and indicates a two phase $LiFePO_4/FePO_4$ system. In addition, the voltage gap between the charging and discharging curves is the smallest in LFP-In-700, which indicates a smaller IR drop *i.e.* greater tolerance to high currents. The highest capacity achieved at 700 $^{\circ}$C can be attributed to the presence of In as well as Fe_2P, which enhance the electronic conductivity. Drop

in capacity of LFP-In-800 compared to LFP-In-700 can be explained on the basis of larger and nonuniform particle size distribution, but it is still better than LFP-In-600, which is due to higher electronic conductivity.

Table 5.1\ Mossbauer parameters of LFP-In-600 and LFP-In-700

	LFP/LA/In-600C	LFP/LA/In-700C	
DOUBLET (1)	**92.2 %**	**86.7%**	Fe^{2+}
DOUBLET (2)	**7.8%**	**8.7%**	**Fe(1) site of Fe_2P**
DOUBLET (3)	**-**	**4.6%**	**Fe(2) site of Fe_2P**
Total Fe_2P	**7.8%**	**13.3%**	
Capacity (mA h/g) at 1C	**140**	**163**	
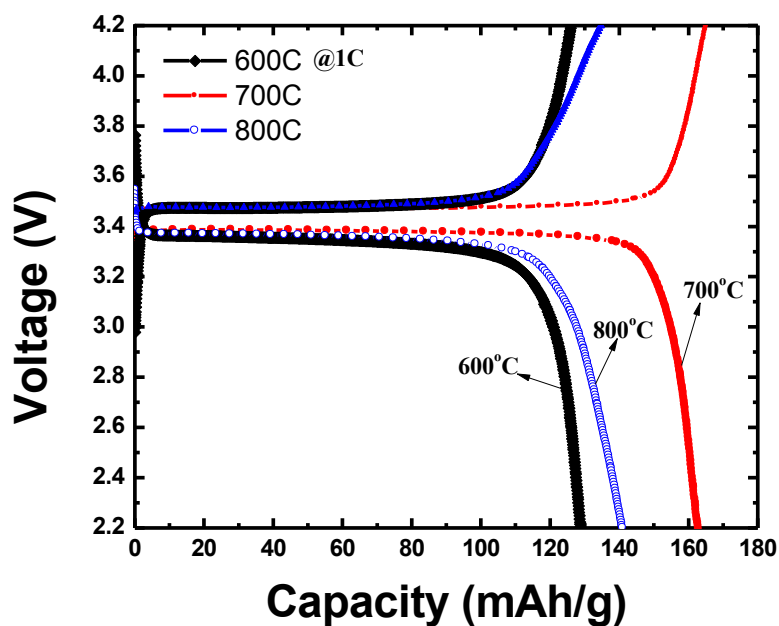
Figure 5.4 Charge discharge profile of LFP-In-600, LFP-In-700 and LFP-In-800 samples

Figure 5.5 displays the charge transfer resistances obtained by electrochemical impedance spectroscopy (EIS). It clearly shows that LFP-In-700 has the lowest charge tranfer resistance followed by LFP-In-800 and LFP-In-600. Finally, the rate capability of all the samples is shown in Figure 5.6. LFP-In-700 shows remarkable capacity at rates 1C, 2C, 5C and 10C. Even at a rate as high as 10C, a capacity of 148 mAh/g is achieved. It is worth noting that capacity depreciation is just 9% as it goes from discharging rate of 1C to 10C. This enhancement can be attributed to improved electronic conductivity provided by both In and the conducting Fe_2P network. LFP-In-600 and LFP-In-800 also shows reasonably good capacity values of 140 mAh/g and 150 mAh/g, respectively, with no appreciable drop when tested at higher rates. There is small amount of Fe_2P in LFP-In-600, but LFP-In-800 did not show any sign of Fe_2P in XRD, suggesting that the performance is enhanced by In doping.
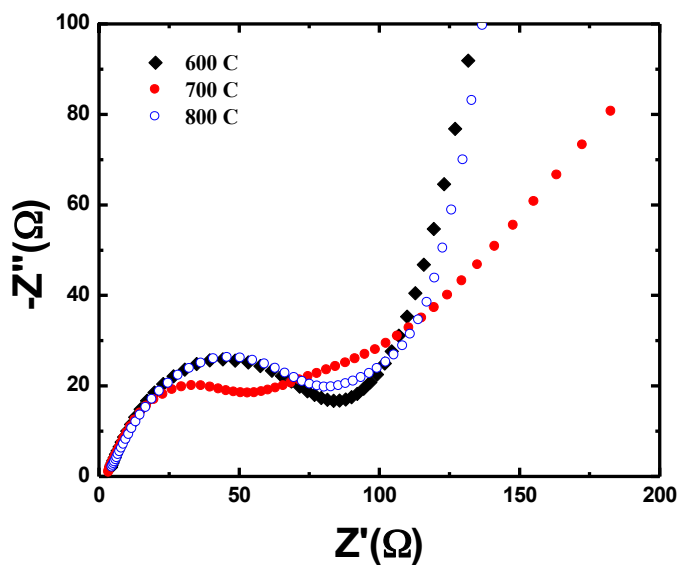
Figure 5.5 EIS of LFP-In-600, LFP-In-700 and LFP-In-800
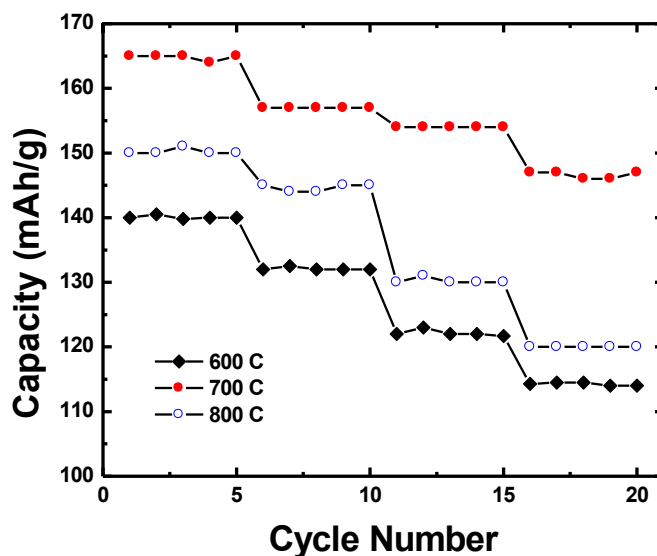
Figure 5.6 Rate capabilities of LFP-In-600, LFP-In-700 and LFP-In-800 starting from left 1C, 2C, 5C and 10C at the right

5.4 Comparison study of LiFePo₄/LA and In-doped LiFePO₄/LA

In Chapter 4, we presented the effect of temperature on the synthesis of LiFePO$_4$ with detailed description of impurities. We found that the presence of iron phosphide (Fe$_2$P) enhances the electronic conductivity and its optimum amount can result in very high specific capacity at relatively high charging rate. It has been found that Fe$_2$P phase appears due to the reducing environment provided by lauric acid and forming gas used during annealing process. In studies presented in Chapter 4 and here in Chapter 5, lauric acid was used as carbon source and Fe$_2$P appears in both studies. Therefore, comparison of the results from these two studies is important in order to see the effects of In doping.

It is clear from the XRD patterns of two sets of samples that there is no X-ray detectable impurity in LFP-600 and LFP-In-600, whereas LFP-700 and LFP-In-700 both exhibit some impurity phase of Fe$_2$P. One unanticipated result from the comparison of XRD patterns of 800 $^\circ$C

calcinated samples is the absence of Fe_2P in LFP-In-800 while it becomes more prominent in LFP-800.
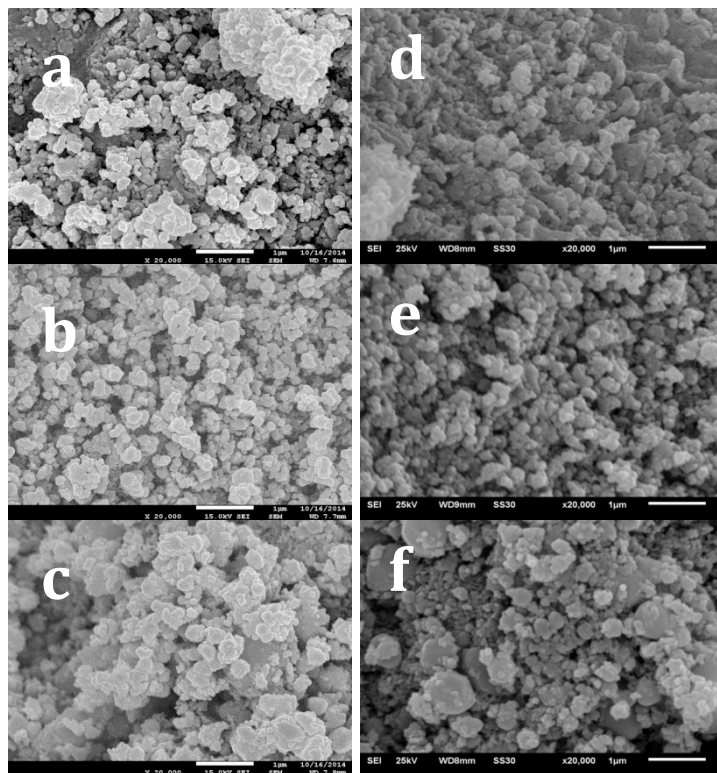
Figure 5.7 SEM images of LFP-In-600-700-800 (5.6(a), (b) and (c))

and LFP-600-700-800 (5.6 (d), (e) and (f))

Figure 5.7 shows SEM images of both LFP-600-800 (5.6 (d), (e) and (f)) and LFPIn600-800 (5.6(a), (b) and (c)) in parallel at same magnification. For samples LFP-600-700 and LFP-In-600-700, there is no noticeable change in morphology with and without indium. However, LFP-800 shows more non-uniformity with some giant particles of size ~ 500nm, while there are very few larger particles in LFP-In-800 indicating that indium may prohibit the particle growth to some extent at higher temperatures, which favors the better electrochemistry.
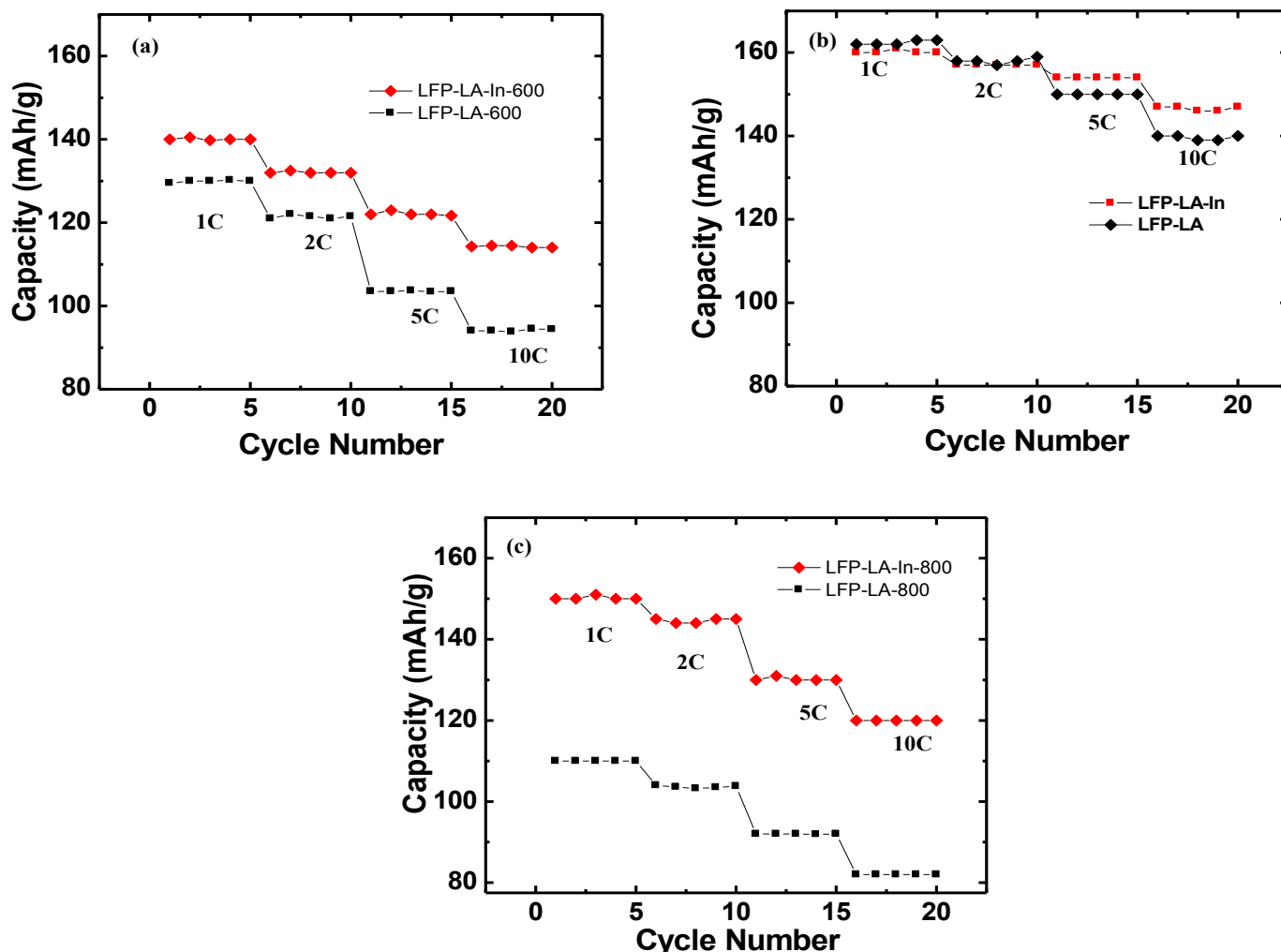
Figure 5.8 Rate capability comparisons of LFP and LFP-In samples annealed at (a) 600 °C, (b) 700 °C and (c) 800 °C at 1C, 2C, 5C and 10C

Figure 5.8 (a), 5.8(b) and 5.8(c) show the rate capabilities of samples annealed at 600 °C, 700 °C and 800 °C with and without indium. Clearly samples annealed at 600 °C and 800 °C with indium show superior rate capability as compared to undoped LFP samples. At 1C LFP-In-600 and LFP-In-800 deliver 140 mAh/g and 150 mAh/g, respectively, while corresponding undoped samples have shown 130 mAh/g and 110 mAh/g, respectively. As shown by Mössbauer spectroscopy, both LFP-600 and LFP-In-600 samples contain almost same amount of Fe_2P, enhanced capacity can be ascribed to possible inclusion of indium in the structure. Although LFP-In-700 shows slightly better capacity at higher rates of 5C and 10C, both samples show almost similar capacity

at low rates. It is likely that electronic conductivity reaches the threshold of Fe_2P in LFP-700 but improved structural stability due to indium might be assisting at higher rates. Figure 5.9 displays the Nyquist plots of different samples.
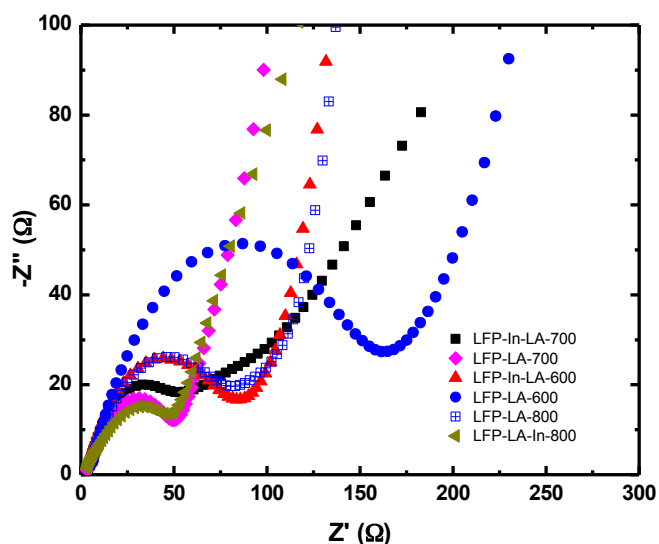
Figure 5.9 Nyquist plots of LFP and LFP-In at different temperatures

An obvious enhancement in electronic conductivity *i.e.* decrease in charge transfer resistance (R_{ct}) can be seen in case of 600 $^{\circ}$C In-doped sample as compared to undoped, which shows better specific capacity. However, R_{ct} for both doped and undoped samples are quite comparable at higher temperatures. Low charge transfer resistances for undoped samples can be associated to the presence of Fe_2P. LFP-800 and LFP-In-800 exhibits almost same charge transfer resistance despite of the fact that XRD did not detect any Fe_2P in LFP-In-800, which means this low R_{ct} is due to the presence of indium. Although, LFP-800 has shown a similar charge transfer resistance as its indium doped counterpart, lower capacity values are observed due to insufficient amount of active material. So all the improvements in electrochemical performance in indium-doped samples can be attributed to the existence of indium in the samples.

To further compare LFP-700 and LFP-In-700, samples were characterized by cyclic voltammetry (CV). Figure 5.10 displays CV curves of LFP-700 (a) and LFP-In-700 (b) at voltage scan rates of 0.2 mV/s to 5 mV/s, respectively. All the curves show a typical redox behavior with anodic current peak and cathodic current peak.
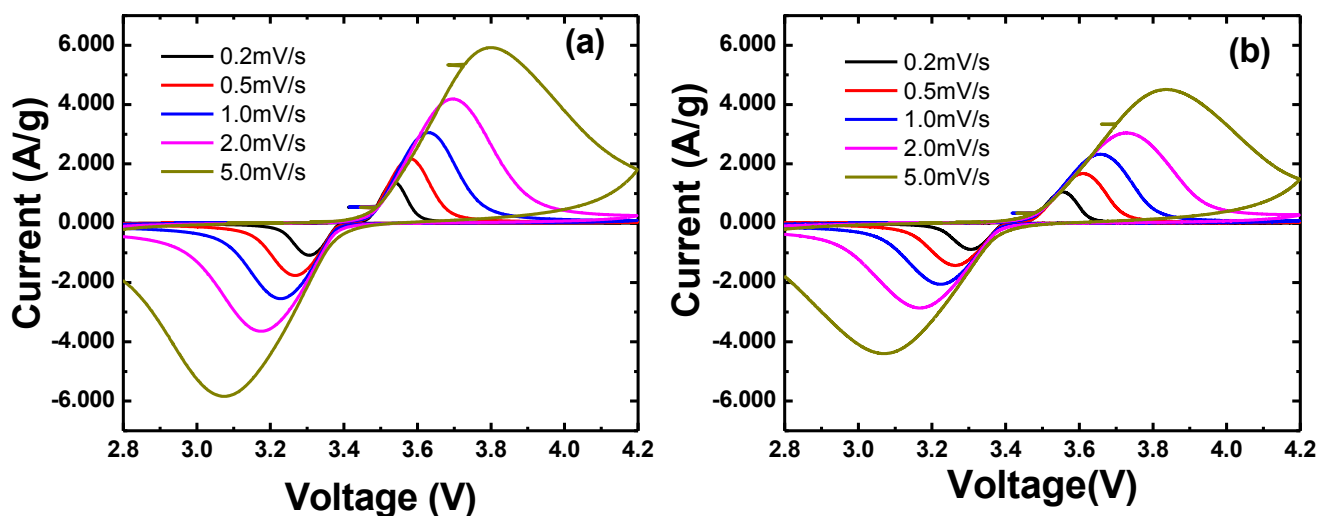
Figure 5.10 Cyclic voltammetry (CV) curves for (a) LFP-700 and (b) LFP-In-700

Peak in each curve represents the highest current obtained during the sweep, so is an indirect estimation of capacity of the material. By looking at the two plots, it is very clear that LFP-In-700 delivers higher peak current during reduction as well as oxidation. Li ion diffusion coefficients can be calculated from square root of scan rates and peak currents using Randals Sevcik equation. The calculated Li-ion diffusion coefficients from Randal Sevcik plot (Figure5.11) are $3.43 \times 10^{-10} cm^2/s$ and $4.67 \times 10^{-10} cm^2/s$ for LFP-600 and LFP-In-700 respectively, which indicate faster kinetics resulting in better capacities at higher rates.
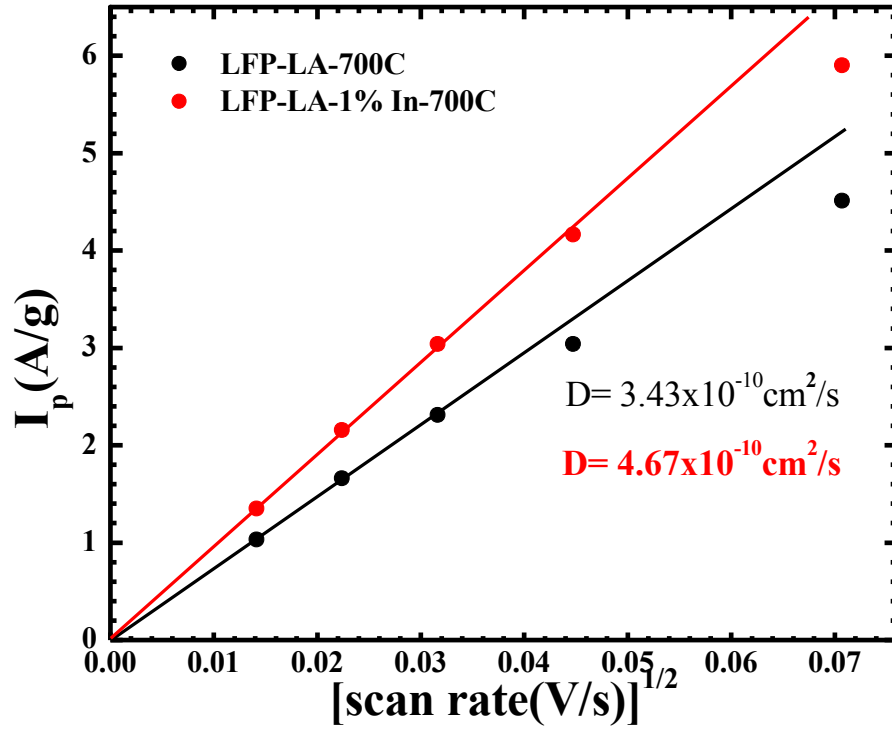
Figure 5.11 Randal Sevcik plot for LFP-LA-700 and LFP-In-700 samples

5.5 Conclusions

We have successfully synthesized In-doped $LiFePO_4$ by sol-gel method. SEM images showed that particles are more uniformly distributed in LFP-In-700 while there is agglomeration in LFP-In-600 and particle growth in LFP-In-800. Although LFP-In-700 contains about 13% Fe_2P, which contributes to electronic conductivity enhancement, better capacities shown by $600^\circ C$ and $800^\circ C$ samples demonstrate the effect of indium. Also cyclic voltammetry results show higher current and faster dynamics in indium-doped samples.

CHAPTER 6

CONCLUSIONS AND FUTURE WORK

6.1 Conclusions

LiFePO$_4$ is a very promising material for Li-ion batteries but suffers from very low electronic conductivity. In this thesis, we presented the methods we developed to enhance the electronic conductivity and electrochemical performance. The results of our investigations are summarized below:

Addition of graphene

In Chapter 3, we have demonstrated that the addition of graphene to LiFePO$_4$ (LFP) enhances electronic conductivity, leading to a significant improvement in capacity and capacity retention of LFP as a cathode material for Li-ion batteries. Annealing at 600 ^{o}C for 5 hrs in Ar/H$_2$ sufficiently reduces the graphene oxide to graphene as confirmed by Raman spectroscopy, electrical conductivity and XPS measurements. Mössbauer spectra confirm that our LFP/G is highly pure with very small amount (~3%) of impurity phases. TEM images of LFP/G show that graphene sheets form a three-dimensional conducting network throughout the sample, providing an easy path for the electrons and Li-ions during the charging/discharging processes. At low C rate, the capacity of LFP/G approaches the theoretical value. More importantly, the LFP/G demonstrates a much better rate capability and drastically improved cyclic stability than LFP. This work suggests that the electrochemical performance of LEP can be substantially improved by adding graphene oxide during the synthesis, even if we do not control the particle size.

Temperature dependence study

We have successfully prepared LiFePO$_4$/C by a sol-gel method followed by calcination at various temperatures. Growth of Fe$_2$P phase in samples prepared at higher temperatures was detected by XRD and magnetic measurements and was quantified by Mössbauer studies. Existance of Fe$_2$P significantly enhances electronic conductivity and hence charge tranfer resistance. Particle size as well as the amount of electrochemically inactive Fe$_2$P grows considerably at 800 ^{o}C and 900 ^{o}C but all the availble lithium can be intercalated because of high electron mobility . LFP-700 contains about 15% of Fe$_2$P, which is sufficient to bring huge improvement in the charge transfer resistance without compromising the quantity of active material. It shows capacity of 160 mAh/g at 1C and 142 mAh/g at 10C with charge transfer resistance of 52 Ω.

Indium Doping

We have successfully synthesized In-doped LiFePO$_4$ by sol-gel method. SEM images showed that particles were more uniformly distributed in LFP-In-700 while there is agglomeration in LFP-In-600 and particle growth in LFP-In-800. LFP-In-700 contains about 13% Fe$_2$P, which contributes to electronic conductivity enhancement resulting in best electrochemical performance among all samples. In case of LFP-In-800, better electrochemical performance can be attributed to In-doping as no Fe$_2$P was detected. So we conclude that LFP-In-700 shows the best performance, which can be ascribed to the presence of both indium and Fe$_2$P, while LFP-In-800's performance improvement over undoped samples is due to the presence of indium.

6.2 Future Work

Effect of Indium Doping

Although we have successfully demonstrated improvement in electrochemical performance of LiFePO$_4$, future work is needed to understand the effect of indium doping. It will be interesting to calculate lattice parameters from XRD pattern to confirm the presence of indium on the iron site. Particle growth control by indium doping is also not clear and needs further investigations.

Synthesis of LiFePO$_4$ using hydrothermal method

In all the studies presented in this thesis, we prepared LiFePO$_4$ using sol gel method, which gives spherical particles. In hydrothermal process, controlling the temperature and pressure conditions can modify the morphology of materials. Making platelet structure using hydrothermal method and studying the effect of graphene and annealing temperature will be interesting.

LiMnPO$_4$ as cathode material

LiMnPO$_4$ exhibits higher voltage than LiFePO$_4$, and hence can provide more energy density. We have successfully synthesized LiMnPO$_4$ using sol gel method. However, it did not show very good performance. Preparing LiMnPO$_4$ using hydrothermal process will be interesting.

REFERENCES

1. Winter, M. and R.J. Brodd, *What are batteries, fuel cells, and supercapacitors?* Chem. Rev., 2004. **104**(10): p. 4245-4270.

2. Ball, R.J., et al., *Failure mechanisms in valve regulated lead/acid batteries for cyclic applications.* J. Power Sources, 2002. **109**(1): p. 189-202.

3. Rand, D.A.J., *Editorial.* J. of Power Sources, 1991. **35**(4): p. v.

4. Endo, M., et al., *Recent development of carbon materials for Li ion batteries.* Carbon, 2000. **38**(2): p. 183-197.

5. Ceder, G., et al., *Identification of cathode materials for lithium batteries guided by first-principles calculations.* Nature, 1998. **392**(6677): p. 694-696.

6. Whittingham, M.S., *Lithium batteries and cathode materials.* Chem. Rev., 2004. **104**(10): p. 4271-4302.

7. Alcantara, R., et al., *Structure and Electrochemical Properties of Boron-Doped $LiCoO_2$.* J. Solid State Chem., 1997. **134**(2): p. 265-273.

8. Amatucci, G.G., J.M. Tarascon, and L.C. Klein, *Cobalt dissolution in LiCoO2-based non-aqueous rechargeable batteries.* Solid State Ionics, 1996. **83**(1–2): p. 167-173.

9. Foll, H., *Defects in Crystals.*

10. Thackeray, M., et al., *Electrochemical extraction of lithium from $LiMn_2O_4$.* Mater. Res. Bull., 1984. **19**(2): p. 179-187.

11. Cabana, J., et al., *Enhanced high rate performance of LiMn$_2$O$_4$ spinel nanoparticles synthesized by a hard-template route.* J. Power Sources, 2007. **166**(2): p. 492-498.

12. Padhi, A.K., K. Nanjundaswamy, and J.B.d. Goodenough, *Phospho olivines as positive ‐ electrode materials for rechargeable lithium batteries.* J. Electrochem. Soc., 1997. **144**(4): p. 1188-1194.

13. Chung, S.-Y., J.T. Bloking, and Y.-M. Chiang, *Electronically conductive phospho-olivines as lithium storage electrodes.* Nat. Mater., 2002. **1**(2): p. 123-128.

14. Andersson, A.S., et al., *Thermal Stability of LiFePO4 ‐ Based Cathodes.* Electrochem. Solid St., 2000. **3**(2): p. 66-68.

15. Laffont, L., et al., *Study of the LiFePO$_4$/FePO$_4$ Two-Phase System by High-Resolution Electron Energy Loss Spectroscopy.* Chem. Mater., 2006. **18**(23): p. 5520-5529.

16. Yonemura, M., et al., *Comparative Kinetic Study of Olivine Li$_x$MPO$_4$ (M = Fe , Mn).* J. Electrochem. Soc., 2004. **151**(9): p. A1352-A1356.

17. N. Ravet, J.B.G., S. Besner, M. Simoneau, P. Hovington, and M. Armand, Abstract 127, The Electrochemical Society and The Electrochemical Society of Japan Meeting Abstracts, 1999. **99**(2).

18. Zhecheva, E., et al., *Particle size distribution and electrochemical properties of LiFePO$_4$ prepared by a freeze-drying method.* J. Phys. Chem. Solids, 2010. **71**(5): p. 848-853.

19. Konarova, M. and I. Taniguchi, *Preparation of carbon coated LiFePO$_4$ by a combination of spray pyrolysis with planetary ball-milling followed by heat treatment and their electrochemical properties.* Powder Technol., 2009. **191**(1): p. 111-116.

20. Hu, C., et al., *Mg Doping of LiFePO$_4$ by co-precipitation for lithium ion batteries.* Int. J. Electrochem. Sci, 2010. **5**: p. 1457-1463.

21.   Herle, P.S., et al., *Nano-network electronic conduction in iron and nickel olivine phosphates.* Nat. Mater., 2004. **3**(3): p. 147-152.

22.   Ou, X.Q., et al., *LiFePO4 doped with magnesium prepared by hydrothermal reaction in glucose solution.* Chinese Chem. Lett., 2008. **19**(3): p. 345-349.

23.   Prosini, P.P., D. Zane, and M. Pasquali, *Improved electrochemical performance of a LiFePO₄-based composite cathode.* Electrochim. Acta, 2001. **46**(23): p. 3517-3523.

24.   Bazzi, K., et al., *Nanostructured high specific capacity C-LiFePO4 cathode material for lithium-ion batteries.* J. Mater. Res., 2012. **27**(02): p. 424-430.

25.   Sides, C.R., et al., *A High-Rate, Nanocomposite LiFePO4/ Carbon Cathode.* Electrochem. Solid St., 2005. **8**(9): p. A484-A487.

26.   Croce, F., et al., *A novel concept for the synthesis of an improved LiFePO₄ lithium battery cathode.* Electrochem. Solid St., 2002. **5**(3): p. A47-A50.

27.   Doeff, M.M., et al., *Effect of surface carbon structure on the electrochemical performance of LiFePO4.* Electrochem. Solid St., 2003. **6**(10): p. A207-A209.

28.   Hu, Y., et al., *Electrochemical performance of sol-gel synthesized LiFePO4 in lithium batteries.* J. Electrochem. Soc., 2004. **151**(8): p. A1279-A1285.

29.   Yang, J. and J.J. Xu, *Nonaqueous sol-gel synthesis of high-performance LiFePO4.* Electrochem. Solid St., 2004. **7**(12): p. A515-A518.

30.   McCammon, C.A., *Insights into phase transformations from Mössbauer spectroscopy.* Rev. Mineralogy and Geochemistry, 2000. **39**(1): p. 241-264.

31.   Dokko, K., et al., *In Situ Raman Spectroscopy of Single Microparticle Li+−Intercalation Electrodes.* J. Phys. Chem. B, 2003. **107**(46): p. 12549-12554.

32.   Delmas, C., et al., *The LixV$_2$O$_5$ system: An overview of the structure modifications induced by the lithium intercalation.* Solid State Ionics, 1994. **69**(3–4): p. 257-264.

33.   Guilmard, M., et al., *Structural and electrochemical properties of LiNi$_{0.7}$0Co$_{0.1}$5Al0.15O$_2$.* Solid State Ionics, 2003. **160**(1–2): p. 39-50.

34.   Dudney, N.J., *Thin film micro-batteries.* Electrochem. Soc. Interface, 2008. **17**(3): p. 44.

35.   Dornbusch, D.A., et al., *Effects of Sonication on EIS Results for Zinc Alkaline Batteries.* ECS Electrochem. Lett., 2013. **2**(9): p. A89-A92.

36.   Rusling, J.F. and S.L. Suib, *Characterizing materials with cyclic voltammetry.* Adv. Mater., 1994. **6**(12): p. 922-930.

37.   Padhi, A.K., K.S. Nanjundaswamy, and J.B. Goodenough, *Phospho‐olivines as Positive‐Electrode Materials for Rechargeable Lithium Batteries.* J. Electrochem. Soc., 1997. **144**(4): p. 1188-1194.

38.   Takahashi, M., et al., *Confirmation of Long-Term Cyclability and High Thermal Stability of LiFePO4 in Prismatic Lithium-Ion Cells.* J. Electrochem. Soc., 2005. **152**(5): p. A899-A904.

39.   Tarascon, J.M. and M. Armand, *Issues and challenges facing rechargeable lithium batteries.* Nature, 2001. **414**(6861): p. 359-367.

40.   Chen, Z. and J.R. Dahn, *Reducing Carbon in LiFePO4 / C Composite Electrodes to Maximize Specific Energy, Volumetric Energy, and Tap Density.* J. Electrochem. Soc., 2002. **149**(9): p. A1184-A1189.

41.   Doeff, M.M., et al., *Optimization of carbon coatings on LiFePO4.* J. Power Sources, 2006. **163**(1): p. 180-184.

42. Dominko, R., et al., *Impact of the Carbon Coating Thickness on the Electrochemical Performance of LiFePO4 / C Composites.* J. Electrochem. Soc., 2005. **152**(3): p. A607-A610.

43. Dominko, R., et al., *Wired Porous Cathode Materials: A Novel Concept for Synthesis of LiFePO4.* Chem. Mater., 2007. **19**(12): p. 2960-2969.

44. Delmas, C., et al., *Lithium deintercalation in LiFePO$_4$ nanoparticles via a domino-cascade model.* Nat. Mater., 2008. **7**(8): p. 665-671.

45. Gibot, P., et al., *Room-temperature single-phase Li insertion/extraction in nanoscale LixFePO4.* Nat. Mater., 2008. **7**(9): p. 741-747.

46. Hsu, K.-F., S.-Y. Tsay, and B.-J. Hwang, *Synthesis and characterization of nano-sized LiFePO$_4$ cathode materials prepared by a citric acid-based sol-gel route.* J. Mater. Chem., 2004. **14**(17): p. 2690-2695.

47. Croce, F., et al., *A Novel Concept for the Synthesis of an Improved LiFePO$_4$ Lithium Battery Cathode.* Electrochem. Solid St., 2002. **5**(3): p. A47-A50.

48. Meethong, N., et al., *Aliovalent Doping for Improved Battery Performance: Aliovalent Substitutions in Olivine Lithium Iron Phosphate and Impact on Structure and Properties (Adv. Funct. Mater. 7/2009).* Adv. Funct. Mater., 2009. **19**(7): p. n/a-n/a.

49. Kim, J.-K., G. Cheruvally, and J.-H. Ahn, *Electrochemical properties of LiFePO$_4$/C synthesized by mechanical activation using sucrose as carbon source.* J. Solid State Electr., 2008. **12**(7-8): p. 799-805.

50. Park, K.S., S.B. Schougaard, and J.B. Goodenough, *Conducting-Polymer/Iron-Redox-Couple Composite Cathodes for Lithium Secondary Batteries.* Adv. Mater., 2007. **19**(6): p. 848-851.

51.   Bauer, E.M., et al., *Versatile Synthesis of Carbon-Rich LiFePO₄ Enhancing Its Electrochemical Properties.* Electrochem. Solid St., 2004. **7**(4): p. A85-A87.

52.   Thorat, I.V., et al., *Performance of carbon-fiber-containing LiFePO4 cathodes for high-power applications.* J. Power Sources, 2006. **162**(1): p. 673-678.

53.   Li, X., et al., *A novel network composite cathode of LiFePO₄/multiwalled carbon nanotubes with high rate capability for lithium ion batteries.* Electrochem. Commun., 2007. **9**(4): p. 663-666.

54.   Geim, A.K. and K.S. Novoselov, *The rise of graphene.* Nat. Mater., 2007. **6**(3): p. 183-191.

55.   Frank, I.W., et al., *Mechanical properties of suspended graphene sheets.* J. Vac. Sci. Technol. B 2007. **25**(6): p. 2558-2561.

56.   Wang, L., et al., *A facile method of preparing mixed conducting LiFePO₄/graphene composites for lithium-ion batteries.* Solid State Ionics, 2010. **181**(37–38): p. 1685-1689.

57.   Zhou, X., et al., *Graphene modified LiFePO₄ cathode materials for high power lithium ion batteries.* J. Mater. Chem., 2011. **21**(10): p. 3353-3358.

58.   Wang, H., et al., *Mn₃O₄–Graphene Hybrid as a High-Capacity Anode Material for Lithium Ion Batteries.* J. Am. Chem. So., 2010. **132**(40): p. 13978-13980.

59.   Zhou, G., et al., *Graphene-Wrapped Fe₃O₄ Anode Material with Improved Reversible Capacity and Cyclic Stability for Lithium Ion Batteries.* Chem. Mater., 2010. **22**(18): p. 5306-5313.

60.   Su, C., et al., *A novel LiFePO$_4$/graphene/carbon composite as a performance-improved cathode material for lithium-ion batteries.* Electrochim. Acta, 2012. **64**(0): p. 190-195.

61.   Shi, Y., et al., *Graphene wrapped LiFePO$_4$/C composites as cathode materials for Li-ion batteries with enhanced rate capability.* J. Mater. Chem., 2012. **22**(32): p. 16465-16470.

62.   Toprakci, O., et al., *LiFePO$_4$ nanoparticles encapsulated in graphene-containing carbon nanofibers for use as energy storage materials.* J. Renewable and Sustainable Energy, 2012. **4**(1): p. 013121-10.

63.   Oh, S.W., et al., *Low temperature synthesis of graphene-wrapped LiFePO$_4$ nanorod cathodes by the polyol method.* J. Mater. Chem., 2012. **22**(33): p. 17215-17221.

64.   Zhang, Y., et al., *A simple solvothermal route to synthesize graphene-modified LiFePO$_4$ cathode for high power lithium ion batteries.* J. Power Sources, 2012. **210**(0): p. 47-53.

65.   Ding, Y., et al., *Preparation of nano-structured LiFePO$_4$/graphene composites by co-precipitation method.* Electrochem. Commun., 2010. **12**(1): p. 10-13.

66.   Su, F.-Y., et al., *Flexible and planar graphene conductive additives for lithium-ion batteries.* J. Mater. Chem., 2010. **20**(43): p. 9644-9650.

67.   Wang, Y., et al., *Synthesis and electrochemical performance of LiFePO$_4$/graphene composites by solid-state reaction.* Mater. Lett., 2012. **71**(0): p. 54-56.

68.   Yang, J., et al., *3D porous LiFePO$_4$/graphene hybrid cathodes with enhanced performance for Li-ion batteries.* J. Power Sources, 2012. **208**(0): p. 340-344.

69. Tang, Y., et al., *Highly conductive three-dimensional graphene for enhancing the rate performance of LiFePO$_4$ cathode.* J. Power Sources, 2012. **203**(0): p. 130-134.

70. Bi, H., et al., *Study of LiFePO$_4$ cathode modified by graphene sheets for high-performance lithium ion batteries.* Electrochim. Acta, 2013. **88**(0): p. 414-420.

71. Lung-Hao Hu, B., et al., *Graphene-modified LiFePO$_4$ cathode for lithium ion battery beyond theoretical capacity.* Nat. Commun., 2013. **4**: p. 1687.

72. Paraguassu, W., et al., *Phonon calculation on olivine-like LiMPO$_4$ (M = Ni, Co, Fe) and Raman scattering of the iron-containing compound.* J. Raman Spectrosc., 2005. **36**(3): p. 213-220.

73. Julien, C.M., et al., *Characterization of the carbon coating onto LiFePO$_4$ particles used in lithium batteries.* J. App. Phys., 2006. **100**(6): p. 063511-063511-7.

74. Doeff, M., et al., *Impact of carbon structure and morphology on the electrochemical performance of LiFePO$_4$/C composites.* J. Solid State Electro., 2008. **12**(7-8): p. 995-1001.

75. Pimenta, M.A., et al., *Studying disorder in graphite-based systems by Raman spectroscopy.* Phys. Chem. Chem. Phys., 2007. **9**(11): p. 1276-1290.

76. Stankovich, S., et al., *Stable aqueous dispersions of graphitic nanoplatelets via the reduction of exfoliated graphite oxide in the presence of poly(sodium 4-styrenesulfonate).* J. Mater. Chem., 2006. **16**(2): p. 155-158.

77. Yumitori, S., *Correlation of C1s chemical state intensities with the O1s intensity in the XPS analysis of anodically oxidized glass-like carbon samples.* J. Mater. Sci., 2000. **35**(1): p. 139-146.

78. Yamada, A., S.C. Chung, and K. Hinokuma *Optimized LiFePO₄ for Lithium Battery Cathodes.* J. Electrochem. Soc., 2001. **148**(3): p. A224-A229.

79. Prince, A.A.M., et al., *Investigation of Fe valence in LiFePO₄ by Mössbauer and XANES spectroscopic techniques.* Solid State Commun., 2004. **132**(7): p. 455-458.

80. Jugović, D., et al., *Preparation of LiFePO₄/C composites by co-precipitation in molten stearic acid.* J. Power Sources, 2011. **196**(10): p. 4613-4618.

81. Hannoyer, B., et al., *Mössbauer study on LiFePO₄ cathode material for lithium ion batteries.* Hyperfine Interac., 2006. **167**(1-3): p. 767-772.

82. Konarova, M. and I. Taniguchi, *Synthesis of carbon-coated LiFePO₄ nanoparticles with high rate performance in lithium secondary batteries.* J. Power Sources, 2010. **195**(11): p. 3661-3667.

83. Shin, H.C., W.I. Cho, and H. Jang, *Electrochemical properties of carbon-coated LiFePO₄ cathode using graphite, carbon black, and acetylene black.* Electrochim. Acta, 2006. **52**(4): p. 1472-1476.

84. Shin, H.C., W.I. Cho, and H. Jang, *Electrochemical properties of the carbon-coated LiFePO4 as a cathode material for lithium-ion secondary batteries.* J. Power Sources, 2006. **159**(2): p. 1383-1388.

85. Huang, H., S.-C. Yin, and L.F. Nazar, *Approaching Theoretical Capacity of LiFePO₄ at Room Temperature at High Rates.* Electrochem. Solid St., 2001. **4**(10): p. A170-A172.

86. Chung, S.-Y., J.T. Bloking, and Y.-M. Chiang, *Electronically conductive phospho-olivines as lithium storage electrodes.* Nat. Mater., 2002. **1**(2): p. 123-128.

87. Ellis, B., et al., *Nanostructured materials for lithium-ion batteries: Surface conductivity vs. bulk ion/electron transport.* Faraday Discuss., 2007. **134**(0): p. 119-141.

88. Lee, K.T. and K.S. Lee, *Electrochemical properties of LiFe$_{0.9}$Mn$_{0.1}$PO$_4$/Fe$_2$P cathode material by mechanical alloying.* J. Power Sources, 2009. **189**(1): p. 435-439.

89. Song, M.-S., et al., *Amphoteric effects of Fe$_2$P on electrochemical performance of lithium iron phosphate–carbon composite synthesized by ball-milling and microwave heating.* J. Power Sources, 2008. **180**(1): p. 546-552.

90. Xu, Y., et al., *Synthesis and effect of forming Fe$_2$P phase on the physics and electrochemical properties of LiFePO$_4$/C materials.* J. Power Sources, 2006. **160**(1): p. 570-576.

91. Qiu, Y., et al., *High-capacity cathode for lithium-ion battery from LiFePO$_4$/(C+ Fe$_2$P) composite nanofibers by electrospinning.* J. Mater. Sc., 2014. **49**(2): p. 504-509.

92. Liu, H., J. Xie, and K. Wang, *Synthesis and characterization of LiFePO$_4$/(C+ Fe$_2$P) composite cathodes.* Solid State Ionics, 2008. **179**(27): p. 1768-1771.

93. Liu, Y., et al., *A novel synthesis of Fe$_2$P–LiFePO$_4$ composites for Li-ion batteries.* J. Appl. Electrochem., 2010. **40**(2): p. 419-425.

94. Rahman, M.M., et al., *LiFePO$_4$–Fe$_2$P–C composite cathode: An environmentally friendly promising electrode material for lithium-ion battery.* J. Power Sources, 2012. **206**: p. 259-266.

95. Kim, C.W., J.S. Park, and K.S. Lee, *Effect of Fe$_2$P on the electron conductivity and electrochemical performance of LiFePO$_4$ synthesized by mechanical alloying using Fe^{3+} raw material.* J. Power Sources, 2006. **163**(1): p. 144-150.

96. Lin, Y., et al., *Effects of carbon coating and iron phosphides on the electrochemical properties of LiFePO$_4$/C.* J. Power Sources, 2008. **184**(2): p. 444-448.

97.   Dhindsa, K.S., et al., *Enhanced electrochemical performance of graphene modified LiFePO₄ cathode material for lithium ion batteries.* Solid State Ionics, 2013. **253**(0): p. 94-100.

98.   Muthuswamy, E., et al., *Control of phase in phosphide nanoparticles produced by metal nanoparticle transformation: Fe₂P and FeP.* ACS Nano, 2009. **3**(8): p. 2383-2393.

99.   Singh, N., P. Khanna, and P. Joy, *Solid state synthesis and room temperature magnetic properties of iron phosphide nanoparticles.* J. Nanopart. Res., 2009. **11**(2): p. 491-497.

100.   Luo, F., et al., *Magnetic and magnetotransport properties of Fe₂P nanocrystallites via a solvothermal route.* J. Mater. Chem., 2004. **14**(1): p. 111-115.

101.   Yamada, A., S.-C. Chung, and K. Hinokuma, *Optimized LiFePO₄ for lithium battery cathodes.* J. Electrochem. Soc., 2001. **148**(3): p. A224-A229.

102.   Prince, A., et al., *Investigation of Fe valence in LiFePO₄ by Mössbauer and XANES spectroscopic techniques.* Solid State commun., 2004. **132**(7): p. 455-458.

103.   Gouveia, D., et al., *Spectroscopic studies of Li x Fe P O ₄ and Li ₓ M ₀.₀₃ Fe ₀.₉₇ P O ₄ (M= Cr, Cu, Al, Ti).* Phys. Rev. B, 2005. **72**(2): p. 024105.

104.   Abbate, M., et al., *Ti-, Al-, and Cu-doping induced gap states in LiFePO₄.* Electrochem. Solid St., 2005. **8**(6): p. A288-A290.

105.   Wang, G., et al., *Physical and electrochemical properties of doped lithium iron phosphate electrodes.* Electrochim. Acta, 2004. **50**(2): p. 443-447.

106.   Liu, H. and J. Xie, *Synthesis and characterization of LiFe₀.₉Mg ₀.₁PO₄/nano-carbon webs composite cathode.* J. Mater. Process Techn., 2009. **209**(1): p. 477-481.

107. Ni, J., et al., *LiFePO$_4$ doped with ions prepared by co-precipitation method.* Mater. Lett., 2005. **59**(18): p. 2361-2365.

108. Liu, H., et al., *Doping effects of zinc on LiFePO$_4$ cathode material for lithium ion batteries.* Electrochem. Commun., 2006. **8**(10): p. 1553-1557.

109. Shenouda, A.Y. and H.K. Liu, *Studies on electrochemical behaviour of zinc-doped LiFePO$_4$ for lithium battery positive electrode.* J. Alloy Comp., 2009. **477**(1): p. 498-503.

110. Shi, S., et al., *Enhancement of electronic conductivity of LiFePO$_4$ by Cr doping and its identification by first-principles calculations.* Phys. Rev. B, 2003. **68**(19): p. 195108.

111. Yang, R., et al., *Characteristics of Li$_{0.98}$Cu$_{0.01}$ FePO $_4$ prepared from improved co-precipitation.* J. Alloy Comp., 2009. **468**(1): p. 365-369.

112. Heo, J., et al., *Synthesis and electrochemical characterizations of dual doped Li $_{1.05}$Fe$_{0.997}$Cu$_{0.003}$PO$_4$.* Mater. Lett., 2009. **63**(6): p. 581-583.

ABSTRACT

ENHANCEMENT IN ELECTROCHEMICAL PERFORMANCE OF LiFePO$_4$-CARBON NANO COMPOSITE MATERIALS FOR LITHIUM ION BATTERIES

by

KULWINDER S. DHINDSA

May 2015

Advisor: Dr. Zhixian Zhou

Co Advisors: Dr. Ratna Naik and Dr. Gholam-Abbas Nazri

Major: Physics (Condensed Matter)

Degree: Doctor of Philosophy

LiFePO$_4$ has attracted great interest as a cathode material for lithium ion batteries due to its reasonably high theoretical capacity (170mAh/g), thermal stability, high Li ion reversibility and low cost. However, prohibitively low electronic conductivity (~10^{-9} S/cm) of LiFePO$_4$ leads to high impedance, low capacity and low rate capability. To overcome this bottleneck, we have developed multiple approaches to improve the conductivity of LiFePO$_4$. Motivated by the outstanding electronic and mechanical properties as well as high surface area of graphene, we prepared LiFePO$_4$/graphene nano-composites by a sol-gel method. The phase purity of the nano LiFePO$_4$/Graphene composite was confirmed by X-Ray diffraction. Addition of graphene improved the electronic conductivity of LiFePO$_4$ by six orders of magnitude. Scanning electron microscopy and transmission electron microscope images show LiFePO$_4$ particles being covered uniformly by graphene sheets throughout the material forming a three-dimensional conducting network. At low currents and charging rate of C/3, the capacity of the composite cathode reaches 160 mAh/g, which is very close to the theoretical limit. More significantly, the LiFePO$_4$-graphene composite shows a dramatically improved rate capability up to 27C and excellent

charge-discharge cycle stability over 500 stable cycles. To further improve the conductivity of $LiFePO_4$ and thus its rate capability, we optimized the concentration of the Fe_2P metallic impurity phase by tuning the annealing temperature. X-ray diffraction shows that samples annealed at 600° C are nearly phase pure while those treated at higher temperatures contain Fe_2P and Li_3PO_4 impurity phases, which increase with increasing annealing temperature. Mössbauer spectroscopy and magnetic measurements were used to quantify the amount of Fe_2P impurity phase. Scanning electron microscopy measurement reveals a noticeable increase in particle size as the annealing temperature increases from 700 ^{o}C to 900 ^{o}C. Optimal results are obtained in $LiFePO_4/C$ samples annealed at 700 ^{o}C, which show the lowest charge transfer resistance, highest Li-ion diffusion coefficient, the highest specific capacity of 166 mAh/g at a rate of 1C and the best rate capability among all samples. In addition, we have also studied the effect of doping In^{3+} on the Fe site and found that the addition of indium significantly improves the electronic conductivity leading to further improvement in capacity and rate capability.

AUTOBIOGRAPHICAL STATEMENT

Education
1. PhD (Physics) Wayne State University, Detroit, Michigan, US -2015
2. M.S. (Physics), Wayne State University, Detroit, Michigan, US-2012
3. M.Sc (Applied Physics-Electronics), G.N.D.U., Punjab, India-2007
4. B.Ed, Panjab University, Chandigarh, India, 2004
5. B.Sc (Physics, Chemistry, Mathematics), Punjabi University Patiala, Punjab, India-2003

Publications

1. "*Enhanced electrochemical performance of graphene modified LiFePO4 cathode material for lithium ion batteries*" **K.S. Dhindsa**, B.P. Mandal, K. Bazzi, MW Lin , M. Nazri, GA Nazri, V.M. Naik, V.K. Garg, A.C. Oliviera, P. Vaishnava, R. Naik and Z. Zhou- **Solid State Ionics 253 (2013) 94-100**

2. "*Nanostructured high specific capacity C-LiFePO$_4$ cathode material for lithium-ion batteries*", K. Bazzi, **K.S. Dhindsa**, A. Dixit, M. B. Sahana, C. Sudakar, M. Nazri, Z. Zhou, P. Vaishnava, V. M. Naik, G. A. Nazri, R. Naik- **Journal of Materials Science, Volume 27 -02 (2012) 424-430**

3. "*Mobility enhancement and highly efficient gating of monolayer MoS2 transistors with polymer electrolyte*", MW Lin, L. Liu, Q. Lan, X. Tan, **K. S. Dhindsa**, P. Zeng, V. M. Naik, M. M. Cheng and Z. Zhou- **Journal of Physics D: Applied Physics- 5 (2012) 345102**

4. "*Electrical transport properties of graphene nanoribbons produced from sonicating graphite in solution*", C. Ling*, G. Setzler*, M.W. Lin*, **K. S. Dhindsa**, J. Jin, H. J. Yoon, S. S. Kim, M. M. Cheng, N. Widjaja and Z. Zhou- **Nanotechnology 22 (2011) 32520** *These authors contributed equally

Conferences and meetings attended
1. Oral presentation at American Physical Society (**APS**), March Meeting 2014, Denver, Colorado
2. Oral presentation at American Physical Society (**APS**), March Meeting 2013, Baltimore, MD
3. Poster presentation at Materials Research Society (**MRS**), Fall meeting, November 2012, Boston, MA
4. Oral presentation at American Physical Society (**APS**), March Meeting 2012, Boston, MA

Fellowships and Awards
1. Summer Dissertation Fellowship from Graduate School Wayne State University, 2014
2. Thomas C. Rumble graduate fellowship from Graduate School Wayne State University, 2013
3. First Prize for poster presentation at Wayne State University Graduate School Research Day 2014